3D-printed porous organic cages for gas filtration: fabrication and flow simulations

Bin Ling, *Rishav Agrawal*, *Donglin He*, *Robert J. Poole*, *Andrew I. Cooper*, *Ming Liu*, and *Esther García-Tuñón**

B. Ling, R. Agrawal, E. García-Tuñón
School of Engineering and Materials Innovation Factory, University of Liverpool, L69 3GH Liverpool, United Kingdom
E-mail: esther.gtunon@liverpool.ac.uk
D. He
Department of Chemistry and Materials Innovation Factory, University of Liverpool, L7 3NY Liverpool, United Kingdom
Prof. R. J. Poole
School of Engineering, University of Liverpool, L69 3GH Liverpool, United Kingdom
Prof. A. I. Cooper
Leverhulme Research Centre for Functional Materials Design, Materials Innovation Factory and Department of Chemistry, University of Liverpool, L7 3NY Liverpool, United Kingdom
Prof. M. Liu
Hangzhou Global Scientific and Technological Innovation Center (HIC), Department of Chemistry, Zhejiang University, 310027 Hangzhou, China.

Keywords: *Porous organic cages, direct ink writing, 3D printing, gas filtration, rheology, gas flow simulations*

Porous organic cages (POCs) are a class of emerging porous materials with high porosity and selectivity for gas adsorption and separation. As a representative of first-generation POCs, CC3 has huge potential for separating noble gases and volatile organic compounds (VOCs). Traditional manufacturing techniques exhibit some limitations in immobilizing the porous materials into structural adsorbents, such as poor transfer efficiency, insufficient loading of active material, limited structural forms, etc. Three-dimensional (3D) printing demonstrates significant advantages in building complex structures with controlled features, to fully exploit their potential. In this study, we demonstrate a versatile approach to 3D print porous materials, successfully shaping CC3 into hierarchical porous architectures by direct ink writing (DIW). Through the rational design of formulations, we obtained inks that combine both printability and functionality, and printed a series of filter prototypes. Tailoring the geometric parameters of the design enables optimizing the gas flow through the structures while minimising energy loss, with the aim to eventually improve the contact and mass transfer between gas and adsorbent. We used computational fluid dynamics (CFD) to numerically investigate the gas flow behaviour through grid-type structures for adsorption applications. Combining bentonite particles and Pluronic F127 hydrogel with CC3 powder enabled the creation of printable formulations that, once dry, retain the functional properties of the cage particles. This formulation approach facilitates the elasto-visco-plastic behaviour required in DIW without damaging the active sites in CC3 crystals. The linear and non-linear elasto-visco-plastic behaviours of formulations with different CC3 concentrations (from 0 wt% to 70 wt%) were characterized by large amplitude oscillatory shear (LAOS) rheology to quantitatively study their printability. The formulation with 50 wt% of CC3 displayed the best printing behaviour in good agreement with the analysis of the LAOS results. The characterisation (scanning electron microscopy, powder X-ray diffraction and surface area measurements (BET)) of multi-scale porous structures evidenced that the CC3 crystalline structure and the adsorption capacity are well preserved. BET surface areas vary with CC3 concentration and can reach up to ≈249 m^2 g^{-1} for 70 wt% CC3. However, high CC3 content also leads to a decrease in shrinkage (≈15% for samples dried in air), higher porosity and low compressive strength ≈0.7 MPa. The CFD simulations on a chosen 2D unit cell reveal the changes of offset distance and porosity significantly manipulate the flow path, velocity distribution and pressure drop through the structures. This work provides a pathway for designing and fabricating hierarchical structures with multi-scale porosity using POCs that can also be widely used for other functional materials and applications.

1 Introduction

Porous organic cages (POCs), formed by discrete covalent-bonded molecules, are a class of emerging porous material with high porosity and attractive properties, such as solution processability, 'mix and match' assembly strategies, rich synthetic diversification, and mobility.[1,2] Equipped with functional molecules and precisely controlled micro-configuration, POCs have demonstrated promising advantages in a wide range of applications, such as adsorption, separation, molecule recognition, catalysis, sensing, and electrochemistry.[3] Rationally-designed POCs can have high selectivity for gas adsorption, such as CO_2, N_2, CH_4, and

hydrogen isotope separation in nuclear fusion applications.[4] As a typical representative of first-generation POCs, CC3 is a regular octahedral crystal with an unimodal limiting pore size of ∼3.6 Å, which is formed by the coordination of 1,3,5-triformylbenzene with trans-1,2-diaminocyclohexane.[5] CC3 with a surface area between 300 and 400 m^2 g^{-1} presented remarkable chemical stability and outstanding potential for separating noble gases and volatile organic compounds (VOCs), such as Xe, Kr, SF_6, formaldehyde and mesitylene.[6,7] Dynamic covalent routes provide a reliable way to synthesize high-yield CC3 powders,[8,9] making possible the industrial and commercial application of POCs. Large-scale synthesis opens up opportunities to realize the potential of CC3 through different processing and manufacturing routes and to bridge the gap between materials discovery and manufacturing.

Directly using CC3 (obtained by the dynamic covalent routes in powder form)[9] in gas adsorption applications has associated risks due to handling fine powders, and limitations due to the difficulty of deployment and recycling. For successful application in filters and other devices, it is necessary to immobilise the powders in a structure while not compromising their adsorption capabilities. Some efforts have already been devoted to processing porous powders into pellets,[10] fibers,[11] and films.[7] Conventional processing techniques such as extrusion,[12] seed growth,[13] molding,[14] and coating[7] have been used to shape Metal Organic Frameworks (MOFs), and POCs. In particular, CC3 fibers have been made recently using electro-spinning.[11] These examples demonstrate the opportunities and challenges of shaping novel porous materials. Despite the progress in this area, the structures made so far exhibit some limitations such as low-pressure drop, poor transfer efficiency, insufficient loading of active species, material loss due to attrition, and limited control of macroscopic features.[15] These limitations clearly hinder the development and widespread application of POCs.

The manufacturing of complex structures with controlled features at multiple scales length made of porous materials (MOFs, POCs, etc.) is essential to exploit their full potential.[16] Thus, advanced processing techniques are in high demand to overcome the challenges mentioned above, and to fabricate complex adsorbent structures with custom-designed 3D architectures.[17] Additive Manufacturing (AM) techniques, often referred to more broadly as 3D printing, have much to offer in this area, including higher customization, design freedom, flexibility and multi-scale architecture control.[18] AM techniques can build more sophisticated designs than conventional approaches through controlled material addition or consolidation.[19] Direct ink writing (DIW), based on the robotic-assisted deposition of a carefully formulated paste,[20] is a promising AM technique for the 3D printing of functional porous materials. DIW builds pre-designed structures layer-by-layer through depositing printable formulations containing a broad range of materials, including advanced ceramics,[21,22] 2D materials,[23–25] and composites.[26–28] DIW is a versatile approach to shape POCs and other porous materials into hierarchical architectures with tailored macrostructure, dimensions, and features for gas filtration and other applications. The challenges to overcome are: the formulation of pastes or inks that meet the rheological requirements for DIW;[22] and producing structures that can be used 'as printed' to retain the intrinsic functional properties of the active materials. There are recent examples of 3D printing organic and inorganic porous materials using DIW: including zeolites,[29] zeolitic imidazolate frameworks (ZIFs),[30] metal-organic (MOFs),[31] and covalent organic frameworks (COFs). Formulation design is key to achieve printability and often requires the addition of surfactants, binders and rheological modifiers, or a multi-functional additive.[32,33] Polymeric binders, such as methylcellulose,[34] 2-hydroxyethyl cellulose,[35] polyvinyl acetate (PVA), polyvinylpyrrolidone (PVP) and Pluronic F127 (F127)[36] are often used in DIW. The problem of these additives is that they lead to a remarkable loss of adsorption performance because the polymer molecules can easily block the nano scale porosity and reduce the specific surface area. Alternatively inorganic additives, such as clays (bentonite,[31] kaolin,[37] or boehmite[38]) can be used as a formulation base thanks to the intrinsic plasticity of clay particle networks.[39] Organic and inorganic additives (clays, cellulose, etc.) can also be combined in certain ratios to form a mixed binder system for example in monoliths made of zeolites,[29,30,40] and MOFs,[31,38,41] to achieve a trade-off between printability, mechanical integrity and functionality. Wang et al[42] and Liu et al[43] have recently developed a binder-free strategy to produce zeolite and COFs monoliths for CO_2 capture. 3D-printed POCs structures with carefully designed features have not been explored yet, however their large-scale synthesis, functional properties, chemical and geometrical versatility make them an excellent candidate for DIW.

The versatility and geometric freedom of DIW makes it possible to manufacture a series of macro-porous structures with customizable geometric features by adjusting parameters such as filament diameter, spacing, orientation, and arrangement. Optimizing the geometric parameters of these macro-porous structures using computational fluid dynamics (CFD) enables us to determine which designs are most promising to achieve enhanced transport properties and adsorption performance. CFD serves as a powerful tool to understand the gas flow behaviour through the structure as a first step to study the gas-adsorbent interactions and optimise mass transfer. For example, a comparative CFD study of velocity distribution through 3D printed structures vs honeycomb extruded monoliths revealed that the interlocking channels of the printed structures led to high-speed regions and turbulence, resulting in better transport properties and contact.[44] Printed structures also outperform extruded honeycomb monoliths in the conversion of CO, methane, and non-methane hydrocarbons.[45] The orientation of different layers at 30° within printed structures can be exploited in methane oxidation to improve conversion rates under turbulent flow.[46] Customized heterogeneous catalysts using 3D-printing demonstrate that control over the internal architecture of non-channelled monoliths enhances mass transfer of reagents and products toward and from active sites due to the regions of turbulent flow inside the flow path.[47] The dimensions of filaments and gaps in grid-type structures also play a role in the gas velocity profile and breakthrough profiles.[48] Gas adsorption and catalysis performance (mass transfer) rely on the contact between active sites and pollutants or reagents and products at the gas/solid interface, which is determined by interconnected factors such as velocity distribution and turbulence regions in the flow path, heat and mass transfer, and pressure drop across the structure.[47,49] These studies emphasised the advantages of CFD simulations to determine how the manipulation of 3D printed structures can be exploited to improve performance by favouring regions of unsteady and/or turbulent flow at small Reynolds numbers that enhance mass and heat transfer.

Here we successfully use DIW to fabricate hierarchical porous architectures made of CC3. This work demonstrates the importance of formulation design to achieve both printability and functional performance. We demonstrate that by combining different additives and solvents it is possible to produce printable formulations while retaining the CC3 adsorption capacity. Using large amplitude oscillatory shear (LAOS) tests we link rheological fingerprints with printability, in good agreement with the observed flow behaviours during the actual printing process. We found that the CC3 crystals play an important role in the rheological behaviour improving printability. Grid type structures with different internal geometries can be made using the formulations with best functional performance according to N_2 adsorption measurements (Brunauer–Emmett–Teller, BET). Structural and chemical characterisation combining different techniques (scanning electron microscopy (SEM), thermo-gravimetric analysis (TGA), and powder x-ray diffraction (XRD)) confirm the preservation of CC3 crystals during formulation, printing and post-processing steps. Mechanical tests in uniaxial compression demonstrated that the post-processing conditions can also be exploited to control the shrinkage and strength of printed structures. The experimental work is combined with CFD simulations to study how the manipulation of the internal geometry of the printed part impacts the flow through the structures (path and streamlines, velocity profiles and pressure drop). This work brings together numerical investigations and additive manufacturing of advanced functional materials, demonstrating the potential of multi-disciplinary research to tackle different challenges such as i) formulation and processing of high-added value materials, ii) complex fluids and rheology, and iii) CFD studies through porous media to bridge the gap between materials discovery and manufacturing.

2 Results and Discussion

2.1 Design of functional CC3 formulations

The formulation of shear-thinning soft solids[33,50] able to yield and flow, to recover in short timescales upon deposition and to retain the desired shape, is critical in DIW to achieve "printability". These yield stress complex fluids must meet three different criteria: *flowability*, *recoverability* and *material strength*.[51] When designing formulations containing new materials in powder form (such as CC3 cages) several factors must be considered to achieve optimal printability: particle size and distribution, morphology (e.g. round or plate-like, smooth or rough surface), composition (surface chemistry), wettability and specific surface.[28]

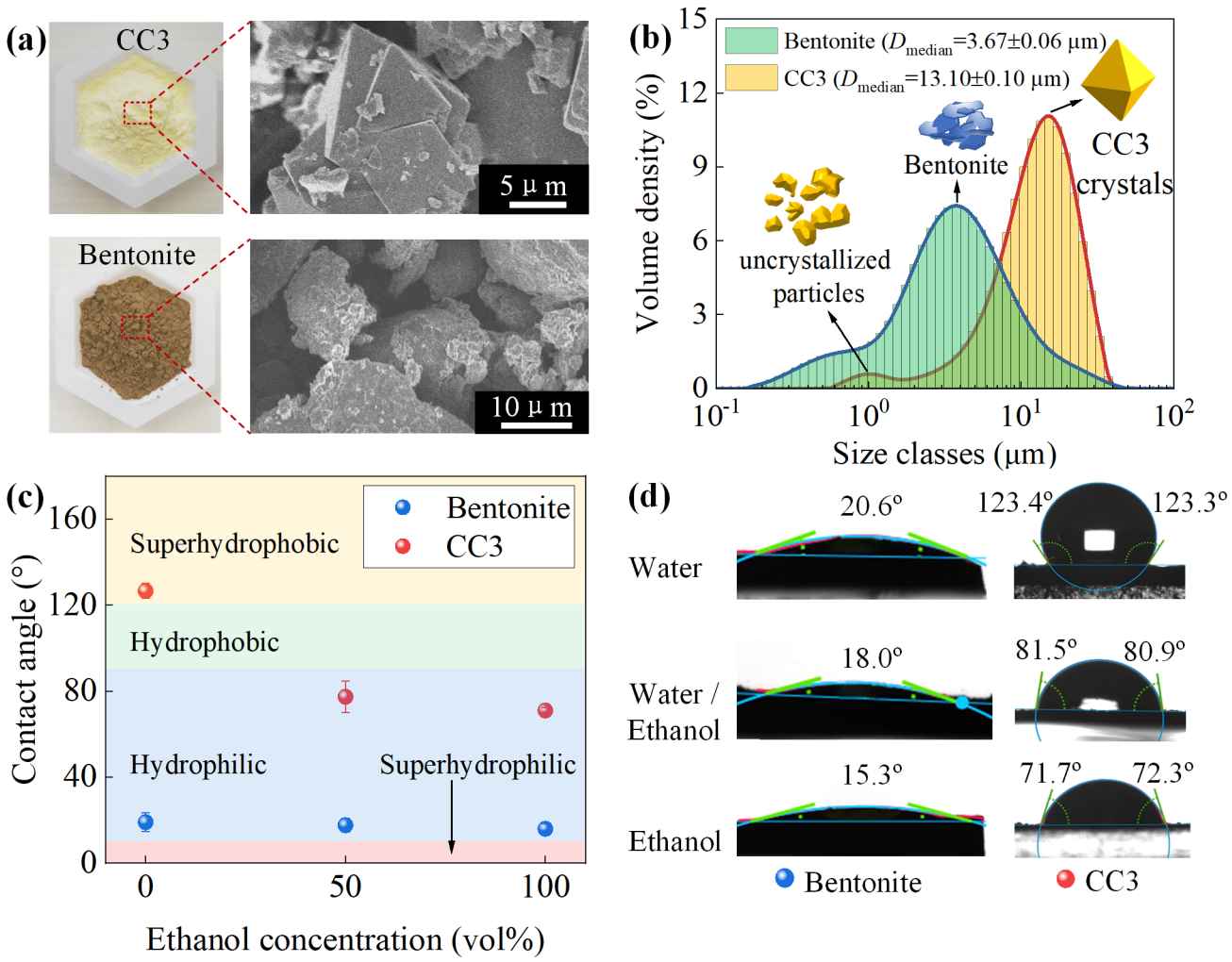

Figure 1: Bentonite and CC3 powder characterisation. (a) Optical and SEM images showing the morphology of CC3 and clay (bentonite) particles; (b) particle size distribution measured with laser diffraction; (c) contact angle values measured using different solvents; and (d) images from the repeated measurements of water, water/ethanol (1:1), and ethanol droplets on the surface of bentonite and CC3 pressed pellets.

The powder's intrinsic properties determine the nature of the interactions between particles, additives (if any) and solvents, which are ultimately responsible for the structure of the complex fluid and its yield-stress, shear thinning behaviour, yielding mechanisms and energy transitions.

The as-synthesized CC3 is a powder with octahedral shaped crystals (Figure 1a) as previously reported[52] and has a bimodal particle size distribution (Figure 1b) that spans over submicron and micro scales with a median particle size of 13.10±0.10 µm. The size distribution curve obtained with laser diffraction (Figure 1b) displays two peaks that correspond to the octahedral crystals (11.06±0.25 µm) and uncrystallized residue (0.58±0.03 µm). The CC3 diamond-shaped particles are relatively large (11.06±0.25 µm) to be affected by Brownian forces and are not expected to behave like colloids; they also have a large surface area (≈428 m^2 g^{-1}). As a typical homochiral organic molecule, CC3 crystals are superhydrophobic with a contact angle of ≈125°±5° with water (Figure 1c and d) which results in low dispersibility and agglomeration in aqueous dispersions.[53] Size, shape and surface chemistry pose a challenge to process CC3 powders into water-based printable formulations in the absence of additives, unlike other materials.[32,43,54] It is not trivial to design a formulation approach that results in the desired printing behaviour without relying on the use of toxic or harmful additives and solvents while preserving the functionality of CC3 crystals. Water based approaches are preferable and commonly used in DIW, containing a variety of additives, surfactants, binders and rheology modifiers. Pluronic F127 hydrogels and graphene oxide (GO) are just two examples

that we have thoroughly used and studied.[50] However, these go-to systems fail to produce successful CC3 formulations that are both printable and functional (Table 1). The definition and quantification of *printability* needs to be made in context, considering the technology used, the processing conditions and the application.[50] Preliminary assessments of *printability* are often made through empirical observations of the flow and material deposition during the printing process. The formulation must be smoothly extruded to form a continuous filament with good shape retention in order to build a good replica of the designed three-dimensional object.[50] Here we used both, empirical assessments for all the formulations studied (Table 1) and quantitative rheological criteria for the optimised formulations (table 2, section 2.2).

When using aqueous Pluronic F127 hydrogels (25 wt%), a well known system in DIW[50] and the soft matter community,[55,56] it is possible to process CC3 into printable formulations (Figure 1). Although F127 provides good printability (Table 1, Figure 2), the active sites and functionality of the CC3 cages are lost with a dramatic decrease in specific surface area from ≈428 m^2 g^{-1} for the CC3 powders to ≈5 m^2 g^{-1} for the F127+CC3 formulation (Table 1). If all the CC3 actives sites were retained, the formulation with ≈73 wt% (Table 1) should have a maximum BET value of ≈311 m^2 g^{-1}. This means that the nano scale porosity is almost completely lost, due to the F127 molecules covering the surface of CC3 crystals and blocking their inner pores. Using GO to create a network of CC3 particles bridged by non-covalent interactions,[32] enables the adsorption capacity to be retained with specific surface area values of ≈176 m^2 g^{-1} for a formulation with 28 wt% CC3 (Table 1). However the GO-CC3 network is not printable due to noticeable clogging and liquid phase segregation at the nozzle tip (also called the 'filter-press' effect (Figure S1)). This suggests that microstructure disruption takes place during the yielding transition,[50] which is likely due to the small size of GO flakes (4.7±1.9 µm) used that limit the formation of a printable gel.[57] Combining GO with bentonite clay particles also did not provide a printable formulation (Figure S1). The same bentonite clay particles in water without additives forms a very stiff but printable formulation. However its behaviour during printing and post-processing is not ideal. The high stiffness and flow stress (quantified in the next subsection) can lead to *flowability* issues during printing, while macroscopic cracking takes place in the drying process. Based on these results, bentonite was selected as the matrix combined with a small amount of F127 (6 wt%). This hybrid formulation base helps to improve the flow properties (*flowability*), and prevent crack formation during the drying process. This approach provides a printable formulation (Figure 2c) that meets printability requirements while retaining functional performance. The adsorption capacity of CC3 powders is preserved (Table 1) with a specific surface area of ≈64 m^2 g^{-1} for a mixture with 20 wt% CC3. Although there is a loss of ≈25% compared to the theoretical value (≈86 m^2 g^{-1} for 20% loading of CC3), it is possible to achieve a compromise between printability and functional performance.

Hybrid formulations contain organic CC3 powders and bentonite-F127 additives in a water/ethanol (1:1) solvent mixture to aid the processing of almost superhydrophobic CC3 powders (Figure 1c). CC3 has good wettability in pure ethanol with contact angle values of 79.1°±4.2° (Figure 1c and d). Using a water and ethanol mixture (1:1), the contact angle of CC3 is 82.7°±2.7° within the hydrophilic region (Figure 1c). CC3 can be easily dispersed in the mixed solvent (water/ethanol, 1:1) to form homogenous formulations containing bentonite and F127. The behaviour observed during printing, and the structural characterisation results demonstrate that these formulations are homogeneously dispersed and stable, without particle agglomerates that could clog the printing nozzle. Using the optimised formulation base (bentonite-F127 matrix in mixed (water/ethanol, 1:1) solvent), we systematically increase the CC3 loading from 0 wt% to 70 wt% (Table 2) with the aim of maximising adsorption capacity, and to optimise the rheological behaviours linked to *printability*. We then investigate structure-property relationships to correlate their *printability*, structural characteristics and functional performance.

2.2 The role of CC3 cage crystals in rheology fingerprints and printability

Successful fabrication via DIW requires the design of formulations that steadily flow through a small diameter nozzle (≈0.5 mm) and form a continuous filament. After printing, the filaments should be stiff enough to maintain their own shape and support the weight of upper layers.[58] The optimised formulations (Table 2) in the previous section are defined as *printable* based on i) visual assessments considering these

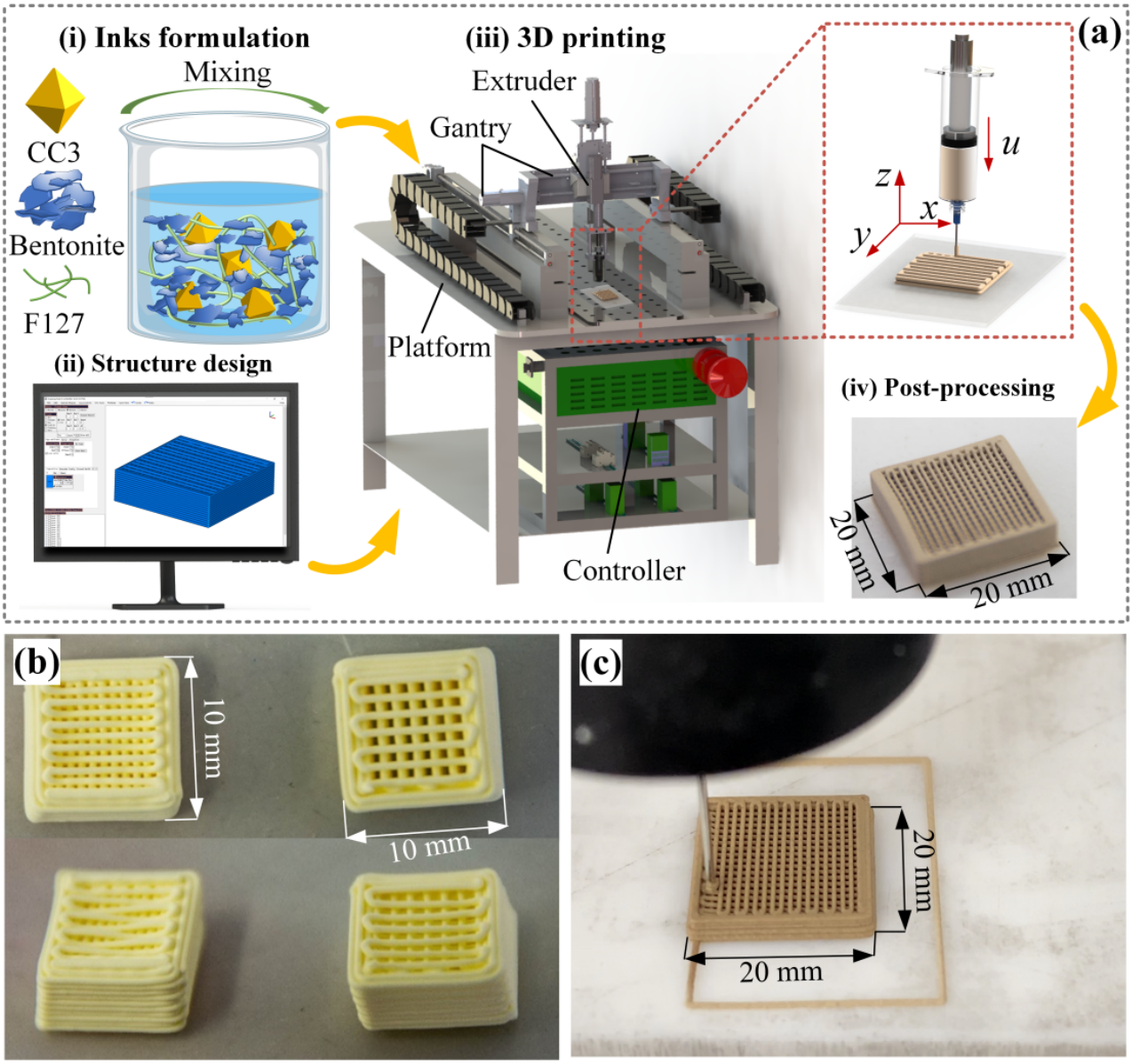

Figure 2: (a) Schematic illustration of the different steps in the processing of 3D-printed CC3 structures with multi-scale porosity. (i) Formulation of printable inks containing CC3, bentonite, F127, ethanol, and deionized water. (ii) Computer-aided design (CAD) of the structure and creating a G-code file. (iii) DIW system (gantry robot with three syringe pumps). (iv) Post-processing involved a drying step to evaporate the solvents. (b and c) Examples of printed parts using different formulations: structures made using F127+CC3, which displayed good printability and shape fidelity (in b); structure made with the optimised formulation (bentonite+F127+CC3) exhibiting good shape fidelity (in c).

Table 1: Printability (empirically assessed) and results of specific surface area (BET measurements) of dry formulations prepared using F127 hydrogels and GO.

Formulation [a]	**CC3 loading**[b] (wt%)	**Printability**	**Specific surface area** (m^2 g^{-1})
(1) F127+CC3	≈73	√	≈5
(2) GO+CC3	28	×	≈176
(3) GO+Bentonite+CC3	20	×	Not tested
(4) Bentonite+F127+CC3	20	√	≈64
CC3 powder	100	—	≈428

Note: (a) Formulations (1-3) were prepared in water, and formulation (4) in water/ethanol (1:1). (b) The CC3 loading is calculated based on dried samples after solvent removal.

Table 2: Composition of formulated inks with varying CC3 loading (where the ratio of bentonite and F127 powder in the matrix is kept fixed to be 3, and the solvent ratio for all of the inks is kept at 46.3 wt%.)

Sample	**Wet formulation**					**Dry sample**		
	CC3 (wt%)	Bentonite (wt%)	F127 (wt%)	Ethanol (wt%)	Water (wt%)	CC3 (wt%)	Bentonite (wt%)	F127 (wt%)
CC3-0	0	50	4	17	29	0	92	8
CC3-20	11	40	3	18	28	20	74	6
CC3-50	27	25	2	20	26	50	46	4
CC3-70	38	15	1	21	25	70	28	2

general requirements and ii) comparing the quality of the printed structure with the pre-designed model. When sagging, collapsing, or deformation of the filaments are obvious, this is generally deemed as poor printability.[59] Assessing *printability* based on visual information only, or by *feel* can be useful, however this descriptive approach can be ambiguous and difficult to characterise, quantify and reproduce. We could be easily misled overlooking other factors to consider such as extrusion settings (rate, nozzle shape, length and material, syringe and tip diameters that will determine the shear rate profiles), microstructure, rheology and even environmental conditions that also play a role. Large amplitude oscillatory shear (LAOS) rheological tests provide a quantitative assessment of printability using linear and non-linear measures to describe the elastic-viscous and plastic flow behaviours of these inks under different strains.[50]

2.2.1 CC3 improves yielding and *flowability*

All the formulations (Table 2) show a type I behaviour[60] with a linear viscoelastic region (LVR) at small strain amplitude values in which storage (G'_{LVR}) and loss moduli (G''_{LVR}) are independent of the strain. As the amplitude increases, both G' and G'' gradually decrease corresponding to strain thinning behaviour.[60] The formulations show a solid-like behaviour in the LVR with G'_{LVR} values greater than G''_{LVR} (Figure 3a). As the CC3 loading increases the formulations become softer and their visco-elastic properties change (Figure 3b). G'_{LVR} values remain similar between 0 and 20% CC3 loading, but they then drop by almost half for 50% and 70% CC3 loading. G''_{LVR} values are roughly the same with no clear trend, while the loss factor ($\tan\delta = G''_{LVR}/G'_{LVR}$) gradually increases with the CC3 loading (Figure 3b). This means that increasing the concentration of CC3 crystals softens the formulations (G'_{LVR} decreases) and enhances the viscous contribution ($\tan\delta$ increases) in the LVR. The yielding transition also changes with CC3 concentration (Figure 3c and d). The stress vs strain amplitude curves show the linear growth in the stress (σ) with increasing strain in the LVR region (Figure 3a). As the strain increases the stress in the material enters the yielding region delimited by the yield point (σ_y) and the maximum (σ_{max}) or bulk flow point (σ_f, corresponding to the crossover point of $G'$and G'' in Figure 3a). Here we estimate the yield point as the yield stress σ_y or yield strain γ_y where G' values decrease to 90% of G'_{LVR}.[33,50] In the yielding region, the formulations soften (G' decreases, figure 3a), and σ values either reach a maximum value σ_{max} or a plateau σ_f (bulk flow) around the critical strain.[50] A maximum in the stress-strain curve is a potential red flag for printability as it can be associated with microstructure disruption during the yielding process,[50] or measurement issues such as fracture, slip or shear banding.[61] The formulation base (0 wt% CC3) shows a maximum in the stress-strain curve (Figure 3c) and extremely high G'_{LVR} and σ_{max} ≈2 kPa values, which can be associated with issues during printing.[50] Bentonite particles form a house-of-cards type network through electrostatic interactions[39] that is responsible for the high stiffness and the maximum values observed in the stress-strain curve. Adding CC3 powders has the beneficial effect of reducing the stiffness and improving the yielding process, which facilitates flow during printing (Figure 3d). Although σ_y values only slightly decrease as CC3 loading increases, σ_{max} remarkably drops by almost half at 20 wt% CC3 and down to ≈500 Pa at 70 wt%. For high CC3 concentrations, the stress-strain curves show a smoother transition to a plateau region that corresponds with bulk flow (σ_f) evidencing a shift in the

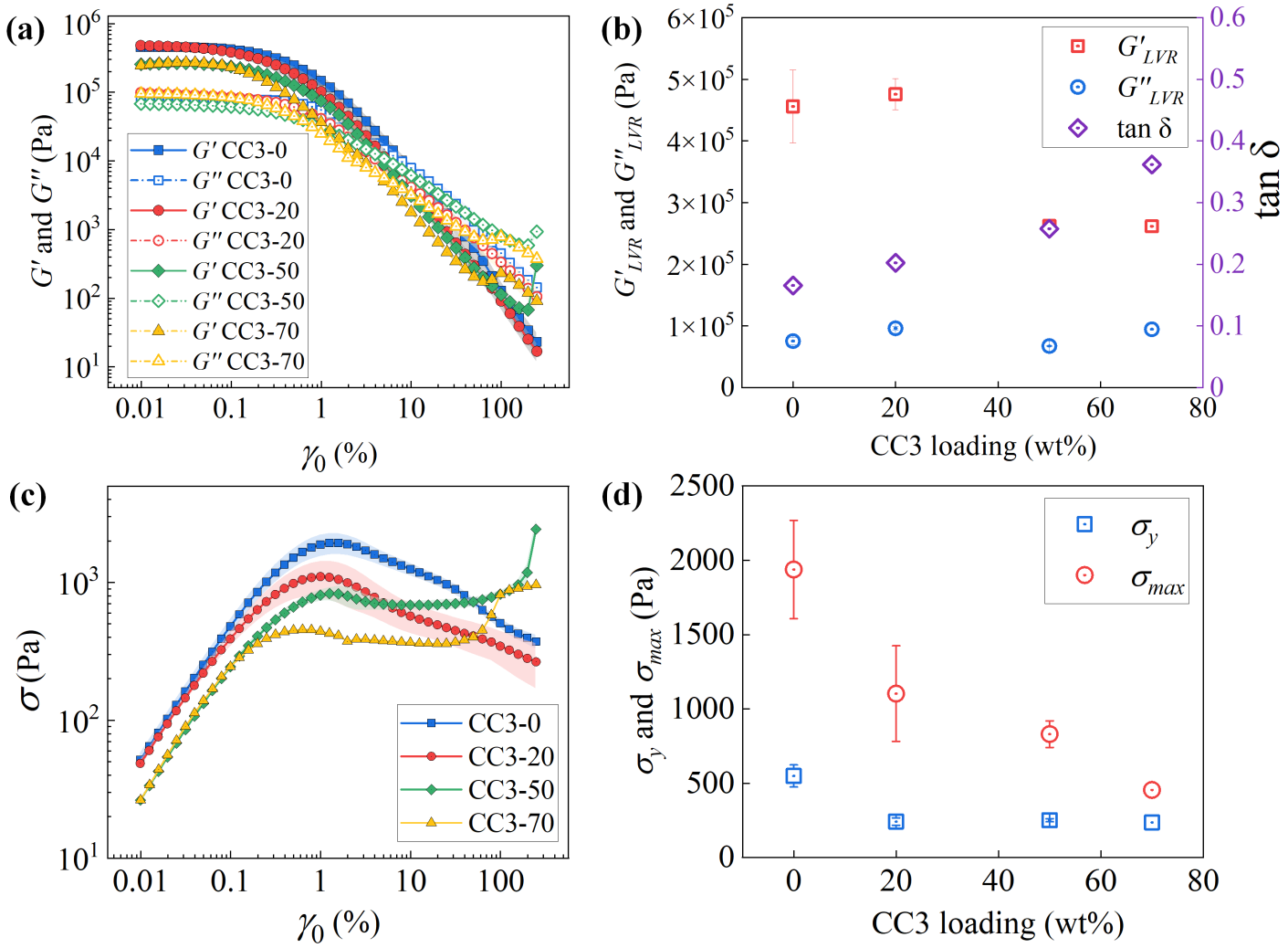

Figure 3: (a) Storage G' and loss G'' moduli (Pa) as a function of strain γ_0 (%) obtained from amplitude sweeps for different CC3 concentrations. (b) Storage G'_{LVR} and loss G''_{LVR} moduli in the linear viscoelastic regime (LVR); and loss factor tanδ, as a function of CC3 loading. (c) Shear stress σ_0 (Pa) as a function of strain amplitude γ_0 (%) at a fixed frequency of 0.5 Hz. (d) Yield stress σ_y (stress value at which G' drops down to 90% of G'_{LVR}) and maximum stress σ_{max} as a function of CC3 loading.

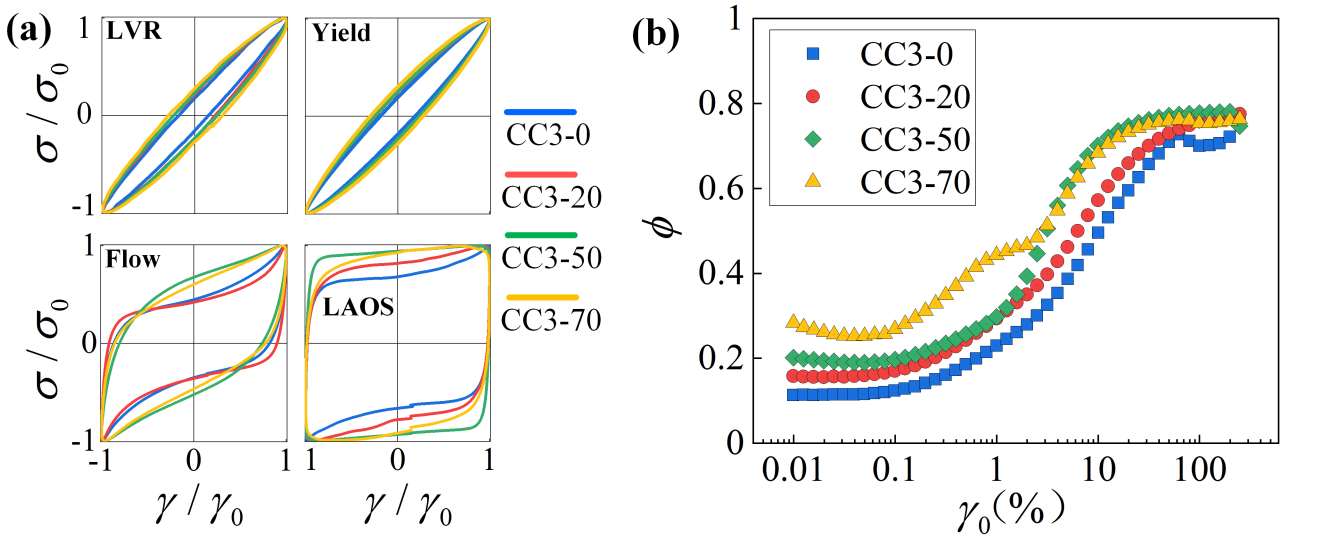

Figure 4: (a) Normalized elastic Lissajous-Bowditch (L-B) curves at different strain amplitudes: LVR ($\gamma_0 = 0.016\%$ for all formulations), yield point ($\gamma_0 = 0.12\%$ for CC3-0, $\gamma_0 = 0.06\%$ for CC3-20, $\gamma_0 = 0.10\%$ for CC3-50, and $\gamma_0 = 0.09\%$ for CC3-70), flow point ($\gamma_0 = 8.50\%$ for CC3-0, $\gamma_0 = 8.74\%$ for CC3-20, $\gamma_0 = 4.20\%$ for CC3-50, and $\gamma_0 = 4.37\%$ for CC3-70), and LAOS ($\gamma_0 = 50\%$ for CC3-0, CC3-20 and CC3-50, and $\gamma_0 = 25.02\%$ for CC3-70). (b) Perfect plastic dissipation ratio ϕ as a function of strain amplitude γ_0 for all formulations.

yielding process. Beyond this plateau region, the stress values rapidly overshoot due to measurement issues at large amplitudes (Figure 3c).[50] These results convey that the cage crystals weaken the network between clay particles by 'getting in the way' and reducing the strong electrostatic interactions. The addition of CC3 to enhance adsorption results in added benefits, softening the formulation, improving the yielding mechanism and as a consequence *flowability*.

2.2.2 Non-linear behaviours and energy transitions

Our analysis and discussion have so far focused on the first harmonic moduli (G' and G'') that only provide information on the linear behaviours, however all the formulations are affected by non-linearities (higher harmonics) in the yielding region (beyond the LVR).[50] Although a complete Fourier Transform (FT) analysis is not within the scope of this manuscript, these behaviours can be visualized using the elastic Lissajous-Bowditch (L-B) curves.[62] The L-B plots show the normalized time-resolved instantaneous stress vs strain at four strain amplitudes (Figure 4a): LVR, yield and flow (the boundaries of the yielding region between the yield and flow points), and LAOS (large amplitude oscillatory shear region). All L-B curves have a narrow ellipsoidal shape in the LVR region that corresponds to predominant solid-like response. As the strain amplitude increases in the yielding region the L-B curves start to deviate from elliptical shape (flow, Figure 3a), due to distortions in the stress raw signals caused by non-linearities.[50,62] The formulations CC3-0 and CC3-20 display the most intense non-linearities. While the L-B curves for CC3-50 and CC3-70, with less distortions and non-linearities overall, get close to being square in the LAOS region (which is an ideal perfect plastic flow behaviour in elasto-visco-plastic materials).[62] These qualitative observations can be quantified using the perfect plastic dissipation ratio (ϕ) to determine the energy transitions (Figure 4b). Values of ϕ close to 0 at small strain amplitudes correspond to predominantly elastic behaviour. As the CC3 concentration increases from 0 to 70 wt%, ϕ values increase from ≈0.1 to ≈0.3 in the LVR region, evidencing a gradual increase of viscous dissipation with CC3 content (in agreement with the trend observed in $\tan\delta$ values). When γ_0 increases, ϕ values change as the formulations yield following different trends, which can be correlated with *printability*. Ideally, DIW formulations behave as elasto-visco-plastic materials (or perfect yield stress soft solids) close to ideal behaviours, from purely elastic (in the LVR) to perfect plastic flow (in the LAOS region).[50,62] This would correspond to ϕ values changing from ≈0 (elastic) to ≈1 (perfect plastic flow) in a narrow region within the intermediate strain range. F127 hydrogels

(25 wt% in water) yield close to these ideal behaviours,[50] undergoing an 'abrupt' yielding process, or in other words behaving like a 'brittle' soft solid.[33] Unlike F127, the bentonite formulation (CC3-0) shows a gradual yielding over a broad strain region with intermediate ϕ values, and a non-monotonic trend at large amplitudes.This means that energy is being dissipated throughout a gradual yielding transition (that deviates from the ideal behaviours), and the material is neither elastic in the LVR nor perfect plastic flow in LAOS. Adding CC3 up to 50 wt% improves the yielding behaviour, with ϕ values transitioning from viscoelastic to a near-plastic flow with increasing γ_0 in a narrow region (Figure 4b). Although the sample with 70 wt% CC3 is the softest (smallest G' values), the non-monotonic trend in ϕ values (even at small strains) highlights some issues in the yielding of this formulation. According to these results, we would predict that the sample CC3-50 is the most suited for DIW with an optimum rheological fingerprint, which is in good agreement with our earlier empirical observations. Thus demonstrating how the results from LAOS analyses can be used to link rheology and *printability* of soft materials.

2.3 Fabrication and characterisation of 3D-printed multi-scale porous structures

Lattice or grid-type structures with different internal features were fabricated following a 4-step manufacturing process (Figure 2). From formulation (i) and structure design (ii) to printing (iii) and post-processing (iv) (scheme in Figure 2a). Different designs can be created by manipulating the distance between filaments in the same layer, and the arrangement of different layers. The simplest design is a grid with regular spacing and identical layers along the z-direction (Figure 2), labelled as *regular* structures ($G = 0$). By shifting the arrangement of filaments in two consecutive layers we created a cubic type lattice, labelled as *offset* structures ($G = 1$ in Figure 8). Thanks to the formulation and rheology optimisation, *regular* and *offset* grid-type lattices were successfully 3D-printed with good shape retention (Figures 5 and 8). The CFD study in the final section of this manuscript provides a comparison of the flow through a wider range of internal geometries with varying offset distances. This enables us to predict which designs are more promising from both a fluid mechanics and mass transfer perspective.

The challenges to preserve the chemical integrity and functional performance of CC3 cages are not unique to formulation design. Another barrier we face is the limited post-processing choices available due to the relatively low decomposition temperature of CC3 crystals (≈322 ℃ according to thermal gravimetric analysis (TGA) Figure 6a). It is therefore not possible to consolidate the structures through any high-temperature process. This means that it is not possible to sinter the clay particles or to carry out a thermal treatment for additive removal. The only post-processing step that can be carried out without compromising the CC3 crystals is controlled drying under different conditions,for example: 1) freeze-drying at -100 ℃(0 bar, for 48 h); or 2) air-drying at room temperature (24 h). Both drying methods are followed by a second heating stage inside a vacuum oven at 80 ℃ (24 h). This vacuum-heating treatment is used to remove residual solvent and activate CC3.[9] Both drying methods can preserve the functional properties leading to different volume shrinkage, apparent densities and mechanical performance (summarised in Table 3, Figures 5 and 7).

2.3.1 Structural characteristics of 3D-printed parts

Drying conditions and CC3 loading have an impact on the dimensions and colour of printed bulk structures, which varies from dark brown to different shades of beige (Figure 5a). This is due to the different shrinkage that the printed parts experience with CC3 concentration and post-processing conditions, which is directly correlated with the structural (apparent density and porosity) and mechanical properties (section 2.3.4). Post-processing does not affect the composition of the structures, the amount of cage remains the same for a given sample, but the drying conditions play an important role in the structural properties. Freeze-drying immediately after printing enables us to preserve the as-printed structure thanks to the rapid freezing of the solvents in liquid nitrogen and the subsequent sublimation process. However air-drying allows a slow evaporation of solvents that results in uncontrolled shrinkage (table 3).

Freeze-drying is a rapid process that leads to minimum shrinkage (as expected). The fast freezing and solvent sublimation minimise volume shrinkage and preserve pores within the filaments (Figure 5f and

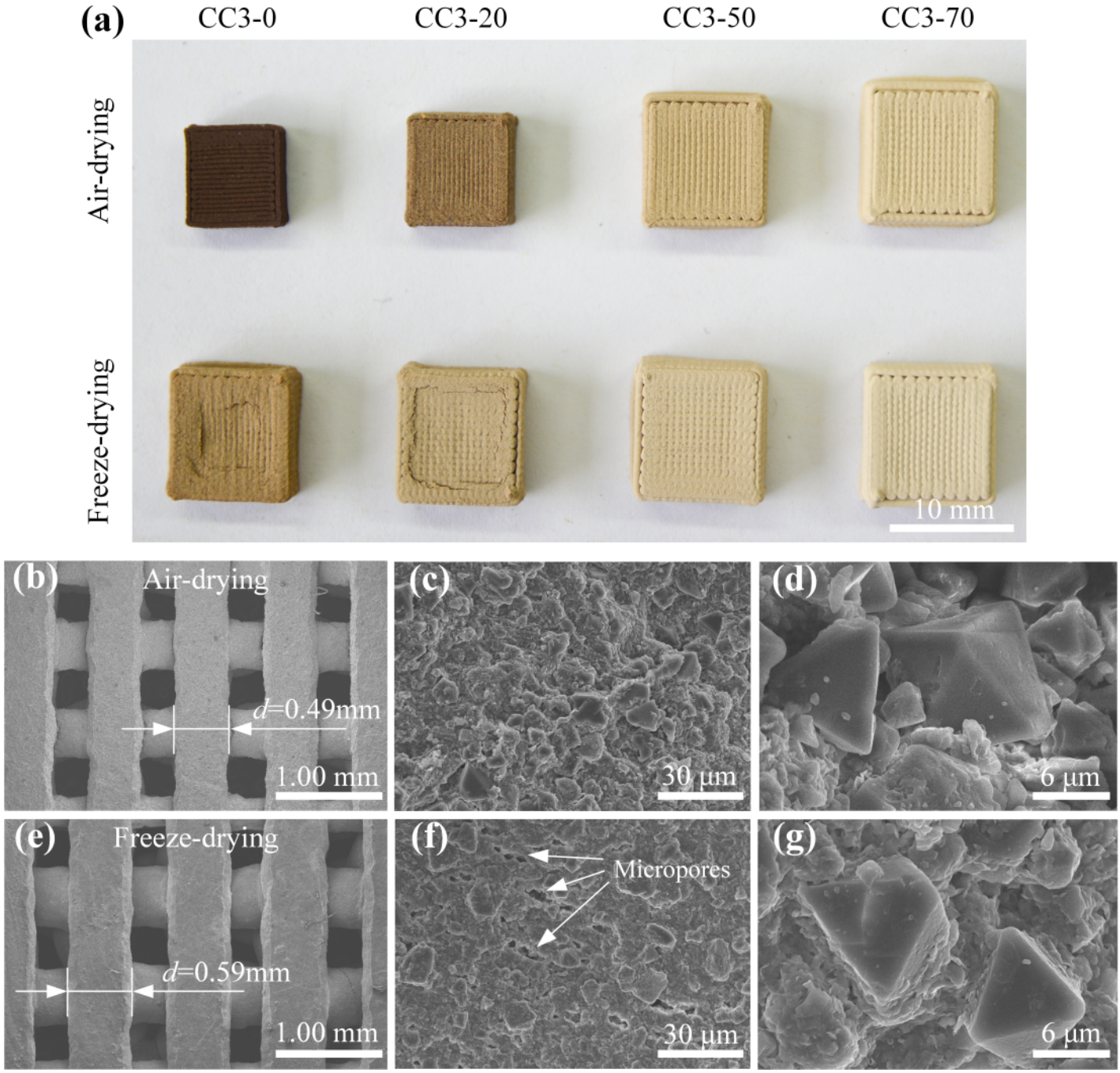

Figure 5: (a) Photographs and SEM images of 3D-printed structures using different drying methods:(b-d) in air at room temperature and (e-g) freeze-drying. Drying in air leads to shrinkage of the structures and increased apparent densities, while freeze-drying preserves the dimensions and porosity of printed parts.

Table 3: Surface area (BET) and structural properties of printed parts fabricated with optimised formulations

Formulation		**Freeze-drying**				**Air-drying**			
	BET	Shrinkage	Apparent density	Porosity	Compressive strength	Shrinkage	Apparent density	Porosity	Compressive strength
	(m^2g^{-1})	(%)	(g cm^{-3})	(%)	(MPa)	(%)	(g cm^{-3})	(%)	(MPa)
CC3-0	≈13	26±2	0.85±0.03	67±1	0.5±0.1	65±1	1.90±0.04	26±1	13±3
CC3-20	≈64	21±2	0.73±0.02	68±1	0.5±0.1	54±1	1.37±0.01	39±1	5.5±0.4
CC3-50	≈177	14±1	0.66±0.01	63±1	0.4±0.1	23±1	0.77±0.01	57±1	1.1±0.1
CC3-70	≈249	7±1	0.56±0.01	62±1	0.3±0.1	15±1	0.60±0.01	56±1	0.9±0.2

g). Freeze-dried bulk monoliths have apparent densities between ≈0.6 and 0.9 g cm^{-3}, corresponding to porosity values between ≈62 and 67% (Table 3).

Air-drying is a slow process that allows the solvents to slowly diffuse and evaporate while the particles come together. The clay structures in the absence of CC3 undergo maximum shrinkage that leads to minimum porosity (≈26 %) due to the de-swelling and aggregation between clay particles.[63] Printed parts dried in air have apparent densities varying between ≈1.9 and 0.6 g cm^{-3}, and porosity values between ≈26 and 57% as CC3 concentration increases from 0 to 70 wt% (Table 3).

CC3 concentration is also playing a role in the structural properties. For both drying methods, the volume shrinkage, apparent density and porosity values seem to correlate with the CC3 content (Table 3). Structures with a high CC3 loading (CC3-50 and CC3-70, Figure 5a) undergo minimal shrinkage even when drying in air. This supports our hypothesis (discussed in section 2.2) on the role of inter-particle interactions in the rheological fingerprints that also affect the drying process. The addition of CC3 powders reduce the electrostatic interactions between clay particles, thus preventing shrinking during the drying process at high concentrations. Higher CC3 loading leads to a decrease in volume shrinkage and apparent density (Figure 5 and 7c). The formulations CC3-50 and CC3-70 exhibit very similar bulk structural properties (shrinkage, apparent density and porosity), however there is a remarkable difference in BET surface areas between them (Table 3).

The structural analyses of grid-type structures from SEM images demonstrates the good shape fidelity achieved through the printing process (Figure 5b-g). Well-preserved diamond-like CC3 crystals (Figure 5d and g) appear homogeneously distributed and embedded within the clay-F127 matrix (Figure 5c and f). The grid-type design of printed structures provides interconnected macro-porosity to facilitate gas flow to and from the CC3 surfaces. The formulation approach and drying process facilitate routes to preserve micro-porosity within the filaments to expose the CC3 active sites. The SEM images taken for structures subjected to different drying methods evidence the impact of the conditions on microstructural features. These structural properties will determine the adsorption capacity and mechanical integrity of printed parts (discussed in sections 2.3.3 and 2.3.4).

2.3.2 Chemical stability of CC3 particles through the manufacturing process

CC3 crystals can undergo different process such as phase transfer, amorphization, chemical degradation, crystal cracking and transformation, among others.[1,9] Structural analyses provided insights into the morphological features of printed parts and to some extent of the CC3 crystals, however additional analyses are needed to quantify their chemical stability, purity and adsorption capacity. Powder X-ray diffraction (PXRD), thermogravimetric analysis (TGA) and Brunauer-Emmett-Teller (BET) results confirm that the CC3 crystals are preserved through the various processing stages, including mixing with additives (F127) and solvents (water and ethanol), extrusion and drying under different conditions.

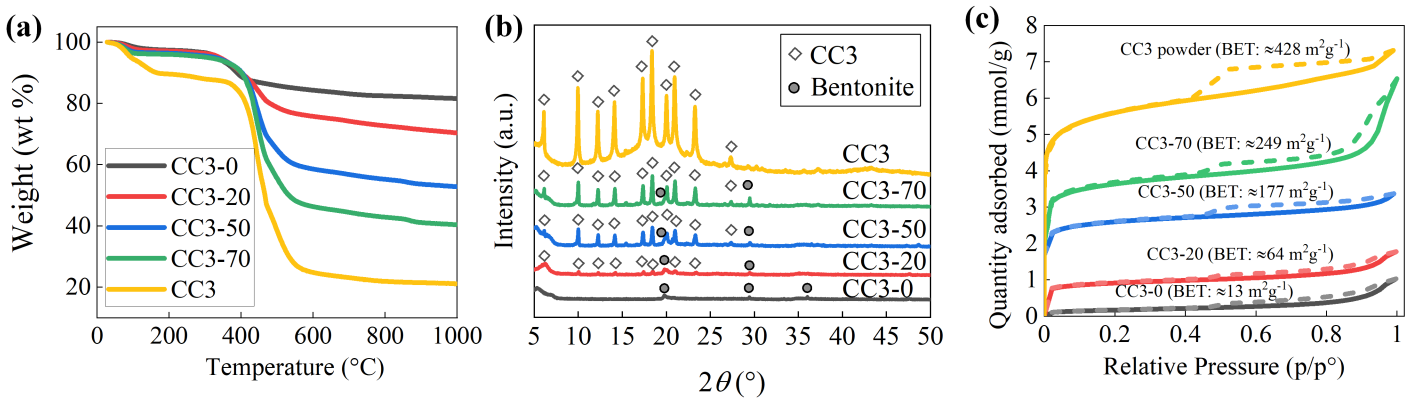

Figure 6: (a) Thermogravimetric analysis (TGA) showing mass changes as a function of temperature. Two stages of weight loss take place in all the samples. (b) Powder X-ray diffractograms (PXRD) of CC3 powders and 3D-printed samples with increasing CC3 loading. The circle symbols highlight characteristic peaks for the montmorillonite pattern at 2θ=19.8°, 29.4°, 36.0° corresponding to planes (001), (100), (005), and (110) respectively.[64] The diamond symbols highlight the main peaks for CC3 at 2θ=6.0°, 10.0°, 12.2°, 14.1°, 17.3°, 18.4°, 20.0°, 20.9°, 23.2°, and 27.3°[5] (c) N_2 adsorption/desorption isotherms of 3D-printed samples using optimised formulations, as measured at -196.2℃. The Brunauer-Emmett-Teller (BET) surface areas derived from the adsorption isotherms are included in the graph.

TGA quantifies the mass changes that dried formulations undergo as a function of temperature. TGA curves show two distinct thermal loss stages for all samples with different CC3 loading (Table S1 and Figure 6a). The loss of physisorbed solvents (first stage) takes place below 200 ℃. CC3 powders have a significant physisorption capacity with a mass loss of ≈10 wt% in this first stage (Table S1). Mass loss for printed samples depends on the amount of CC3 in the formulation (Table S1 and Figure 6a). As the temperature increases, CC3 powders undergo thermal decomposition between ≈322 ℃ to ≈652 ℃ with a mass loss of ≈64 wt%. CC3-0 is relatively stable with a mass loss of 10 wt% between 284∼450 ℃, attributed to the dehydroxylation of the aluminosilicate in bentonite[65] and the decomposition of F127. The mass loss in the second stage for dried formulations and the residues at 1000 ℃ also vary with the concentration of CC3. From the TGA results it is clear that any heat treatment at ≈300 ℃ would result in the undesired thermal decomposition of CC3 and as a consequence in the loss of adsorption capacity.

PXRD results rule out any potential phase transition or amorphization (Figure 6b) during the manufacturing process. The diffraction pattern for CC3 powders confirms their composition and crystallinity, with well-defined peaks.[5] As expected, the intensity of CC3 peaks increases with concentration (Figure 6b) for the different formulations. The characteristic peaks for CC3 and bentonite (montmorillonite[64]) are identified in the diffraction patterns of all formulations. TGA and XRD analyses confirm that CC3 crystals are well preserved through the formulation, printing and post-processing stages.

2.3.3 Adsorption properties of optimised formulations

Gas adsorption (N_2) measurements for hybrid (bentonite+F127+CC3) formulations showed that the surface area is directly correlated with CC3 content (Figure 6c). Apparent BET surface areas increase from ≈13 m^2 g^{-1} for the formulation base (CC3-0; bentonite have little adsorption capacity) up to ≈249 m^2 g^{-1} for the highest CC3 loading (CC3-70) (Figure 6c). The addition of CC3 considerably increases BET values, however the nanoscale porosity of pure CC3 (≈428 m^2 g^{-1}) is not fully preserved in the formulations. This is attributed to the presence of additives that might fill, obstruct, or cover some of the pores. The shape of the isotherms slightly change with CC3 content. The formulations with CC3 concentrations up to 50 wt% (CC3-0, CC3-20 and CC3-50) seem to follow a classic type I behaviour.[8] The isotherm for the raw (as-received) CC3 powder (and to some extent, for the CC3-70 formulation) seem to deviate from type I and hysteresis is observed. Although there is a loss of the adsorption capacity due to the formulation process, overall we have achieved a good compromise between processing, printability, and porosity to produce hierarchical porous structures using DIW.

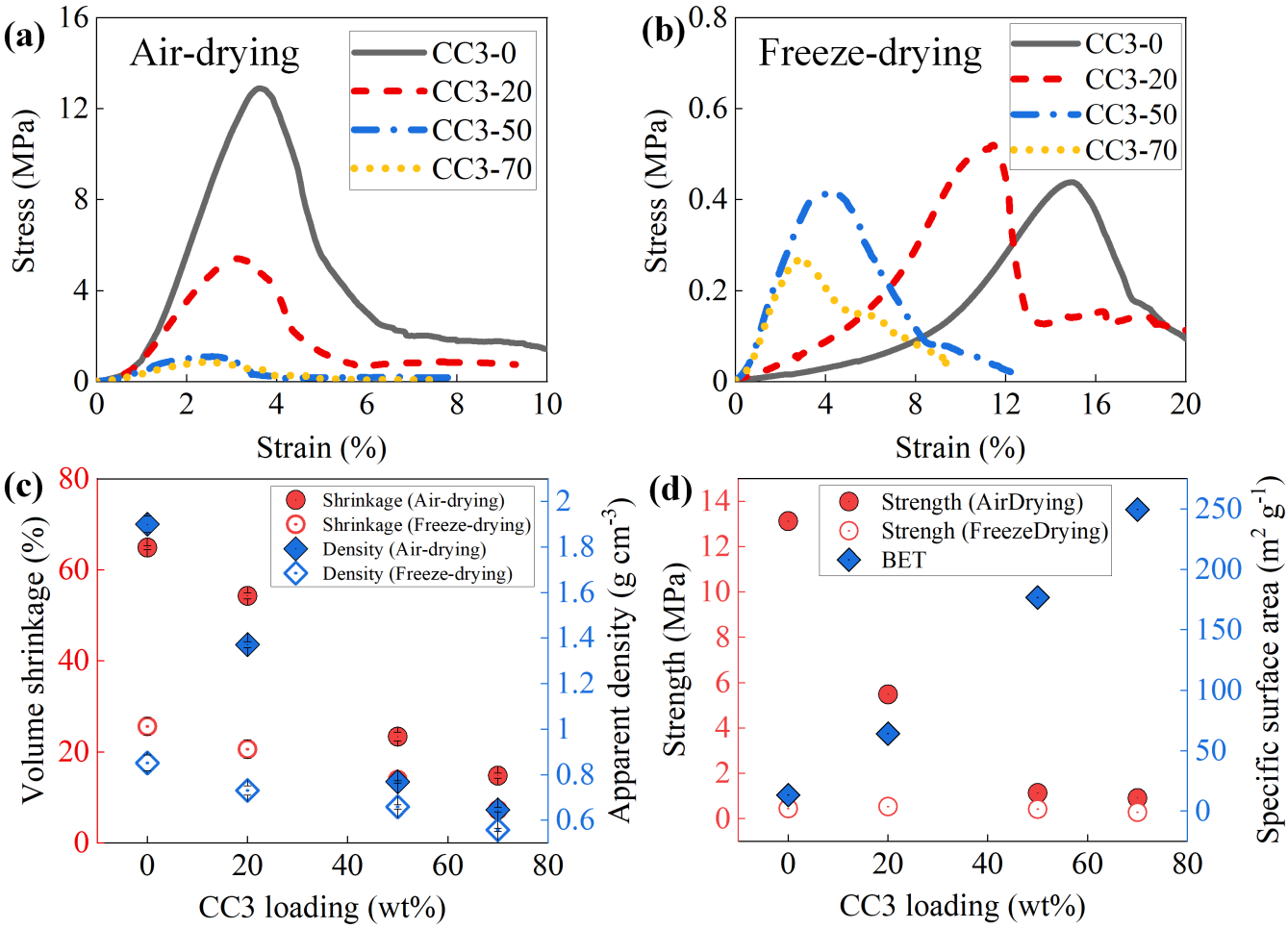

Figure 7: Compression tests results for 3D-printed bulk cylindrical monoliths following the American Society for Testing and Materials (ASTM) standard.[66] Compressive stress-strain for specimens post-processed by (a) drying in air vs (b) freeze-drying. (c) Volume shrinkage and apparent density. (d) Compressive strength and BET surface area vs CC3 loading.

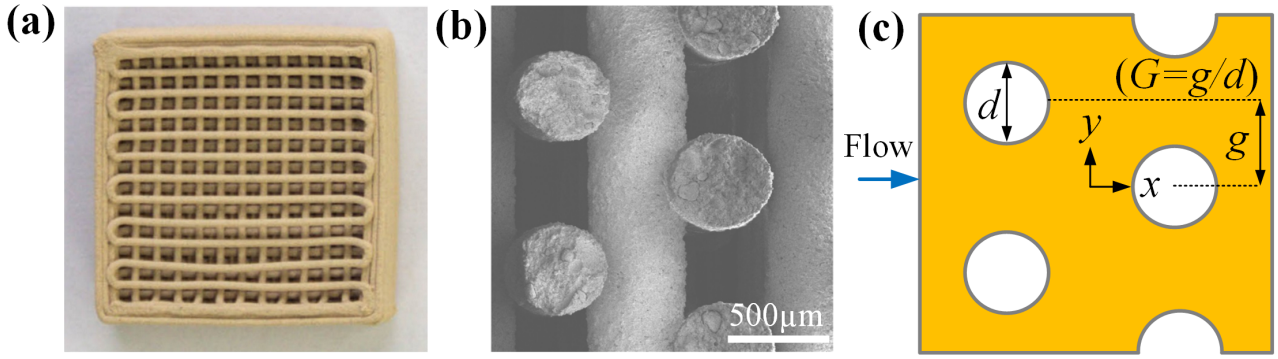

Figure 8: (a) Image of a 3D-printed porous structure using the formulation CC3-50 subjected to freeze-drying. (b) SEM image of its cross-section ($G = g/d = 1$), where gas flows horizontally through the channels created by the cylindrical filaments. (c) Geometry of representative 2D unit cell where the offset distance between filaments, g is 0.5 mm with dimensionless parameter $G = 1$.

2.3.4 Mechanical performance of 3D-printed monoliths

Compression tests[66] demonstrate a clear correlation between the mechanical properties (compressive strength) and apparent density values (or volume shrinkage),[67] which vary with drying conditions and CC3 content (discussed in section 2.3.1). Stress-strain curves for 3D-printed bulk monoliths subjected to drying at room temperature show a strong dependency on CC3 loading (Figure 7a). As CC3 concentration increases from 0 wt% to 70 wt%, the maximum compressive strength decreases from ≈13 MPa to ≈0.7 MPa, and the stiffness drops from ≈2 MPa to ≈0.3 MPa. This is due to the considerable differences in shrinkage and apparent density values between the samples. A printed CC3-0 part shrunk down to ≈65 % when dried in air due to several physicochemical processes taking place during drying, including de-swelling and particle aggregation.[63] The considerable shrinkage that this sample undergoes results in an increase of apparent density, a dark brown colour (Figure 5a) and low porosity (≈26 %). This as a consequence leads to compressive strength values of 13±1 MPa, the highest amongst all the samples (Figure 7d). As CC3 concentration increases, homogeneously distributed CC3 particles within the formulation matrix create obstacles secluding the clays and limiting aggregation, similarly to sand networks in bentonite soils.[63] Printed bentonite-F127-CC3 monoliths undergo considerably less shrinkage as CC3 content increases (Table 3, Figures 5a and 7c)). The porosity increases with CC3 loading and as a consequence the compressive strength decreases (dropping below 1 MPa for CC3-70). Shrinkage, apparent density and compressive strength values for bulk samples subjected to freeze-drying (Figure 5b) show the same trend with CC3 loading (Figure 5c). Drying conditions make a big difference at low CC3 concentrations (at and below 20wt%, Table 3 and Figure 7). However for concentrations of 50wt% and above (CC3-50 and CC3-70) bulk samples show similar compressive strengths independently of drying conditions. CC3-50 and CC3-70 printed monoliths with porosities between ≈57±1 % and 63±1 % have compressive strengths values that range from ≈0.2 to ≈1 MPa (Table 3, Figure 7). These samples are delicate with poor mechanical integrity.

From a structural and functional perspective, there is a trade-off between apparent density, mechanical integrity and BET surface area results (Figure 7d). The samples with the highest adsorption capacity (CC3-50 and CC3-70) also display the lowest mechanical integrity with similar strengths to those reported for printed MOF monoliths.[31] The results suggest that the best compromise to improve mechanical performance (if needed) could be achieved at intermediate concentrations (in between CC3-20 and CC3-50) and drying in air after printing. Overall, we demonstrate that it is possible to create bentonite-CC3 3D structures that retain high BET surface area, while providing enough binding between CC3 particles to enable practical use. A key benefit of this approach is the ability to manipulate gas flow paths through structures with different designs, thus enhancing contact between pollutants and active sites. CFD studies complement the experiments here reported demonstrating the value of using simulations to guide the design of 3D-printed filters (section 2.4).

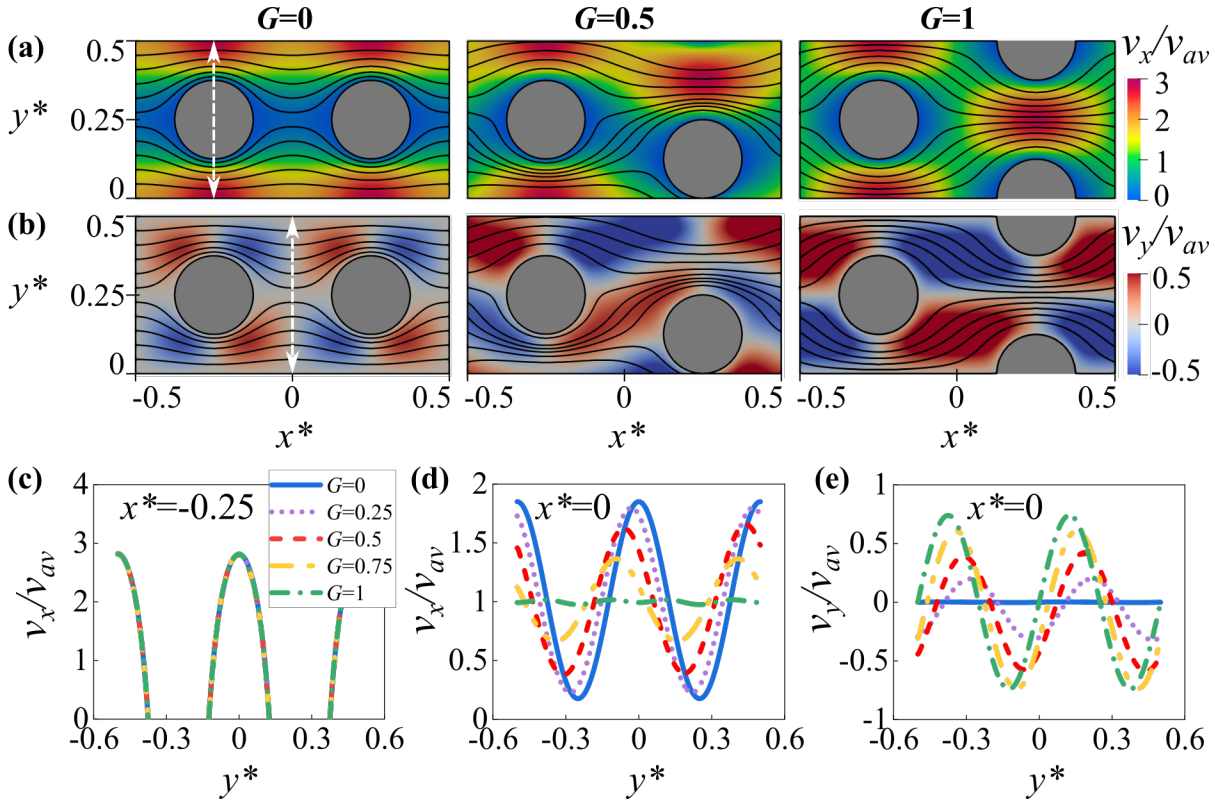

Figure 9: (a) v_x/v_{av} and (b) v_y/v_{av} velocity contours with streamlines superimposed for solid geometries with $G = 0$, $G = 0.5$ and $G = 1$ (left to right) at $Re = 0.1$. (c) v_x/v_{av} profile along the vertical line $x^* = -0.25$ (dashed line in Figure 9a). (d) v_x/v_{av} and (e) v_y/v_{av} profiles in the middle of the unit cell, at $x^* = 0$ (dashed line in Figure 9b). The G values legend is the same for the graphs in c, d and e.

2.4 CFD flow simulations through structures with different internal geometries and porosities

CFD simulations make it possible to study the flow through structures with different geometries and porosities. The internal architecture of hierarchical structures can be easily tailored through both, formulation and CAD design steps. For example by changing the CC3 loading it is possible to tune the porosity (ε), and the geometry can be tailored by changing the space between filaments (g), and their arrangement in different layers (G, Figure 8).

2.4.1 Flow through structures with dense filaments

Practical examples of 3D-printed structures with G (offset distance g normalized by the diameter of the filament d, $G = g/d$)) values of 0 (regular grid) and 1 (cubic type arrangement), evidence the capability of the DIW process to control this dimensionless parameter (Figure 2 and 8). CFD simulations enable us to determine which designs (with different G values from 0 to 1) could enhance adsorption performance. Manipulating the streamlines and favouring regions of instabilities and increased tortuosity at small Reynolds number (Re) can enhance mass and heat transfer.[47] Here we set Re=0.1 ($Re = \rho v_{av} d/\mu$ section 4.6) which is a value within the range used in practical adsorption applications.[17,29,47]

Velocity contours (v_x/v_{av}) with superimposed streamlines for solid geometries with different G values illustrate the changes in flow path and velocity distribution (Figure 9a). The gas flows through almost straight 'channels' between the gaps in regular grids with $G = 0$ and with very low values of v_y. The high-speed regions are located in channels along the x-direction in between filaments (red areas in Figure 9a left). Low-speed regions are distributed in front of and behind the cylinders (regions in blue, Figure 9a left). With an increase in G, this channelling effect is suppressed and eventually disappears for $G = 1$ (Figure 9a). The high-speed regions split as the flow paths bend around the cylinders with increasing G

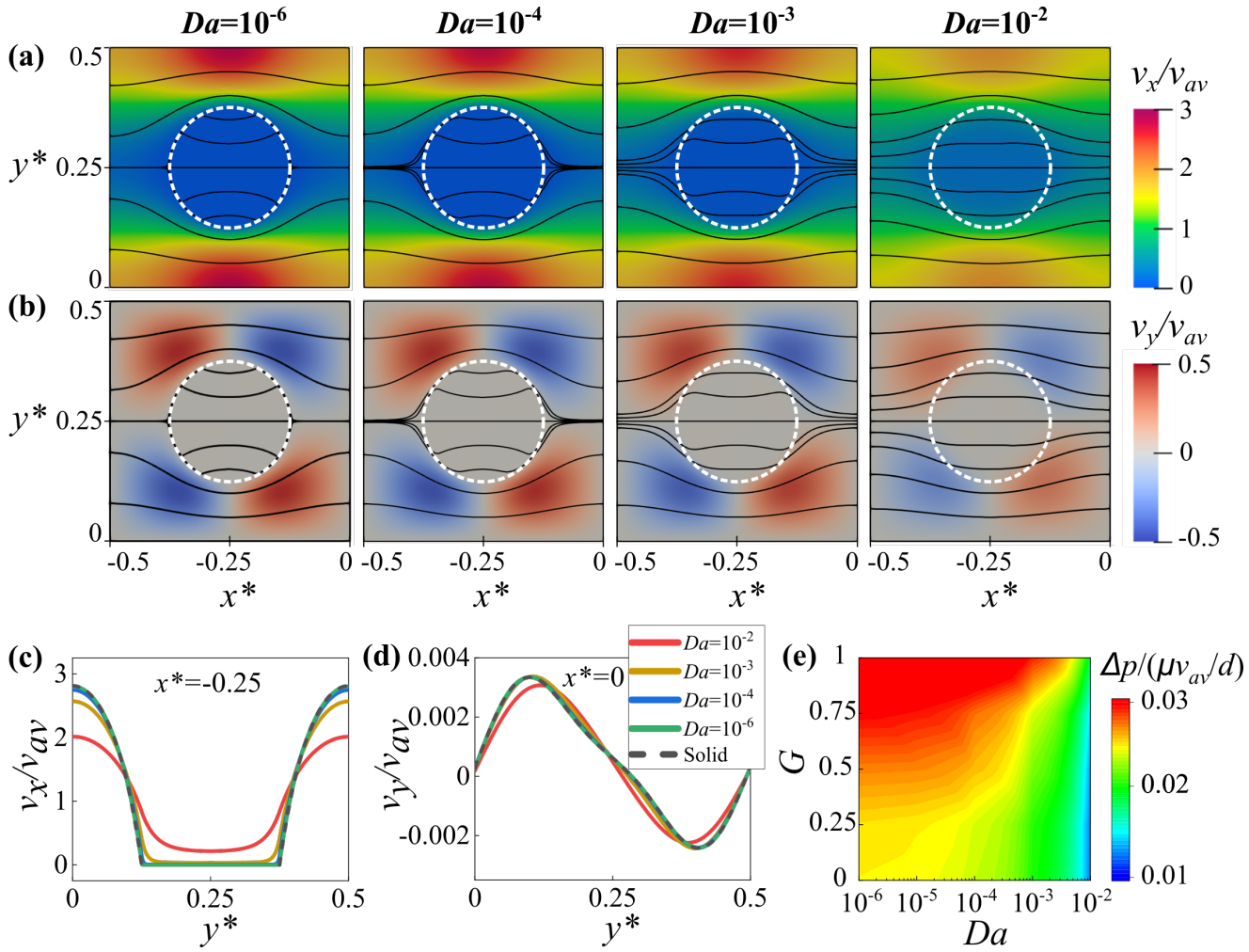

Figure 10: (a) v_x/v_{av} and (b) v_y/v_{av} velocity contours with streamlines superimposed around porous cylinders (with $Da = 10^{-6}$, $Da = 10^{-4}$, $Da = 10^{-3}$, and $Da = 10^{-2}$) for geometry $G = 0$ at $Re = 0.1$.(c) v_x/v_{av} profile along the vertical line $x^* = -0.25$ (dashed line in Figure 9a). (d) v_y/v_{av} profiles at $x^* = 0$ (dashed line in Figure 9b). The legend is the same for the graphs in c and d.(e) Normalized pressure drop ($\Delta p/(\mu v_{av}/d)$) as a function of Da and G.

values. Although the v_x/v_{av} profiles in the gap between adjacent filaments (at x^* = -0.25) show that the velocity distribution in these high speed regions remain the same for different G values (Figure 9c), there is a substantial change in both velocity profiles (v_x/v_{av} and v_y/v_{av}, Figure 9d and e) and streamlines (Figure 9a and b) in the middle of the unit cell ($x^* = 0$). The vertical velocity component increases in magnitude (Figure 9e) and area (Figure 9b), and the horizontal velocity component decreases in magnitude (Figure 9d) at $x^* = 0$ as the filaments shift towards the maximum offset ($G = 1$).

These results demonstrate that changing the parameter G does have the desired impact on flow path manipulation. The increase in G leads to curved streamlines (Figure 9a and b), which increase the length of the flow path and facilitate contact between gas and adsorbent.[49,68] This trend can contribute towards the overall enhancement of transport properties.[17]

2.4.2 Flow through structures with porous filaments

The structural analyses demonstrated that the porosity of the filaments depends on the formulation design (CC3 concentration) and to some extent, on the drying conditions (section 2.3.1). CFD simulations also enable us to systematically study the role of the filament's porosity in the flow physics. The Darcy number Da is commonly used to describe the flow characteristics through porous media.[69] Da accounts for the effects of both material properties and flow parameters. Da can be calculated based on the porosity (ε) using the Kozen–Carmen model[70] ($Da = \frac{1}{180}\frac{\varepsilon^3 d_p^2}{(1-\varepsilon)^2 d^2}$, where the particle diameter d_p of the porous medium

is approximately 5 µm, similar to the particle size observed in Figure 5c and f, and d is the diameter of the filament).

CFD results for Da values from 10^{-6} (ε=0.63) to 10^{-2} (ε=0.99)) for G=0 show how the velocity contours and pressure drop change with the porosity of the filament (Figure 10). When Da increases the v_x/v_{av} contour around the cylinder boundary changes; the streamlines now can get through the cylinder and gradually become more straight (Figure 10a) due to the increased permeability of the cylinder. The contours for the horizontal velocity component (v_x/v_{av}, Figure 10) show the lowest speed regions inside the filaments, which would enhance mass transfer between the flowing gas and the POCs by increasing the residence time. The vertical velocity component (v_y/v_{av}) contours split into four areas with positive and negative values around the boundaries of the cylinder (Figure 10b). When Da values increase, the velocity gradients in both contours v_x/v_{av} and v_y/v_{av} become less intense (Figure 10a and b). The velocity profiles at x^* = -0.25 (Figure 10c) show that they become smoother as Da values increase, and that they remain very similar at $x^* = 0$ (Figure 10d).

The results show that both G and Da can be tuned to manipulate the flow path and velocity contours, however increasing G or decreasing Da can also cause a rise in the pressure drop between the inlet and outlet (Figure 10e). This is primarily due to the viscous resistance that the gas encounters to get around the cylindrical obstacles, resulting in increased energy loss. For any Da value, the pressure drop increases when G values change from 0 to 1 (Figure 10e, Table S3). The relative pressure drop of a solid geometry increases by ≈35 %, while this increase is ≈53 % for a porous geometry with $Da = 10^{-2}$ (Table S3). The maximum pressure drop takes place at Da=10^{-6} (small ε) and G=1. At a given G value, an increase of porosity ($Da \uparrow$) leads to a decrease of pressure drop (Figure 10e).

The CFD analysis here presented (for a 'unit cell' within the 2D geometry at a set Re of 0.1) evidences the potential of such simulations to achieve a compromise between flow properties and pressure drop through multi-scale porous structures, and to optimise 3D printing designs for adsorption and catalysis. Although fully 3D and transient simulations are beyond the scope of this manuscript, they are powerful tools to further develop a multi-disciplinary research area at the interface between materials chemistry and engineering.

3 Summary and practical implications

The formulation and 3D printing strategies here reported enable the fabrication of architectures with hierarchical porosity. The lattice structures designed via CAD and fabricated by DIW offer customizable millimetre-scale (or hundreds of microns) pores, while individual filaments within the lattice provide micrometer-scale pores (at this level, porosity can be adjusted through formulation design and post-processing conditions). At the molecular level, CC3 cages provide nanometre-scale cavities that can be tuned via functional groups and crystal packing.[7] The demonstrated ability to fabricate structures with tunable multi-scale porosity provides new avenues for optimizing material performance, fluid dynamics, and adsorption behaviour in practical applications. This optimization has the potential to address some of the limitations found in packed or fixed bed systems. For example, Borne et al[11] found that in a Xe/Kr adsorption and separation experiment, CC3-containing fibres packed in a fixed bed resulted in smaller pressure drop and higher mass transfer rate compared to pellets with the same CC3 loading. In both types of packed bed, the fibres or pellets are randomly stacked and lack effective means of adjustment. The hierarchically porous architecture demonstrated here offers a more precise customization of gas flow pathways, thus enabling additional opportunities for practical applications and performance enhancement.

Beyond gas filtration, POCs stand out due to their tunability, modularity, and processability that can be exploited in a wide range of industrial applications, such as sustainable environment, catalysis, energy and sensors to name but a few.[71] By adjusting the pore size and shape of POCs, specific gas pairs can

be selectively absorbed and separated, such as H_2/N_2, H_2/CO, CH_4/N_2, Xe/Kr, SF_6/N_2 and D_2/H_2.[72,73] For example, in nuclear fusion applications, Liu et al.[4] combined small-pore and large-pore cages together to achieve an excellent deuterium/hydrogen selectivity with high deuterium uptake (up to 4.7 millimoles per gram). In proton exchange membrane fuel cells, the structure of POCs facilitate a three-dimensional pathway for proton conduction with enhanced conductivity up to 10^{-3} S cm^{-1} at high relative humidity.[74] As catalytic supports, POCs loaded with transition metal catalysts have shown outstanding reactivity, dispersibility, stability, and reusability.[75] In short, the tunable molecular-level design of POCs makes it possible to exploit their diverse functionalities in different applications. This work demonstrates the successful fabrication of 3D printed CC3 architectures with controlled porosity at multiple levels, while retaining the adsorption capacity. Successfully combining both molecular-level design of POCs and 3D printing can further advance their practical industrial applications.

4 Conclusions

Using direct ink writing, we have developed a versatile approach to 3D print CC3 (a class of POCs) and create hierarchical architectures with pore sizes ranging from macro to nano scales. The macro-porosity is determined by the 3D design that can be optimised using CFD simulations to manipulate flow properties. The micro-porosity within the filaments is determined by the formulation and post-processing approaches that preserve CC3 particles within a clay matrix. At the molecular level, POCs provide a versatile platform to tune the selectivity and uptake for different applications. Retaining the adsorption capacity of POCs through the formulation, printing and post-processing stages is challenging. Our work addresses a research gap and demonstrates the successful fabrication of porous architectures made of CC3 via direct ink writing (DIW). The contributions of this work can be summarised as follows: i) Successfully developing a printable CC3 (POCs) formulation for direct ink writing (DIW) that retains significant adsorption capacity. Using bentonite and F127 hydrogels in ethanol and water, we achieved printable formulations with CC3 concentrations up to 70 wt%. ii) Achieving new insights and fundamental understanding into the role that CC3 plays in the rheological behaviour and printability using large amplitude oscillatory shear (LAOS). We found that the addition of CC3 to the bentonite-F127 mixture improves the rheological behaviour required for DIW. The formulation with 50 wt% CC3 displayed the best flow and shape retention during the printing process in agreement with LAOS results. iii) Fabricating hierarchical structures made of POCs with controlled porosity at different levels (which could be extended to other functional materials). SEM, TGA and PXRD confirmed the preservation and stability of the chemical composition and crystalline structure of CC3 during the formulation, printing and post-processing steps. BET surface areas can reach ≈249 m^2 g^{-1} for 70 wt% CC3. Although N_2 adsorption measurements confirmed that the adsorption capacity increases with CC3 loading, a high CC3 concentration (50 wt% and above) also leads to lower apparent densities and weak mechanical integrity. Post-processing steps, air vs freeze-drying, do also play a role in the final structural properties, leading to different apparent densities and compressive strengths. And iv) combining the experimental work with CFD simulations to understand the role of the design parameters in the flow path and velocity contours, which pave the way for adsorption optimization.

The systematic formulation study, combined with the rheological fingerprints and the functional and structural characterisation, highlight the central role that CC3 particles play in every step through the manufacturing process. From improving the yielding behaviour and flow during printing, to altering the physicochemical processes taking place in the post-processing stages. Our multi-disciplinary approach demonstrates the importance of fundamental studies to optimise the processing of advanced functional materials and to realise their potential from discovery to manufacturing. CFD flow simulations complement the experimental research, and provide a promising route to optimise DIW designs for gas filtration and more broadly for any applications that require control of porosity and geometry at multiple scale lengths.

5 Materials and methods

5.1 Materials

CC3 was synthesized following a large-scale synthesis approach.[1,11] Bentonite was purchased from Inoxia Co., Ltd. (UK). Both CC3 and bentonite powders were sieved through a 106 µm stainless steel mesh (6229536, Retsch) in a powder cabinet. Pluronic F127 was purchased from Sigma Aldrich and used as received.

5.2 Formulation process

A representative processing sequence for the CC3-20 formulation is described as follows. An aqueous F127 stock solution (7.5 g, 25 wt%) was firstly prepared by adding F127 powder into a polytetrafluoroethylene (PTFE) jar of deionized water in an ice bath. Small amounts of F127 powders were added under continuous stirring until they were completely dissolved. The solution was mixed at 2000 rpm for 2 minutes in a THIARE250 planetary mixer, and then cooled down for 2 minutes to prevent overheating. The mixing-cooling cycles were repeated several times until a smooth and transparent gel at room temperature was achieved. Once ready, the stock solution was stored in the fridge at ∼4 °C. Sieved CC3 powders (1.6 g) were slowly added into an water/ethanol (1:1, 5.5 g), and mixed in a THIARE250 mixer at 2000 rpm for 2 minutes. The F127 stock solution (2 g) was added into the suspension and mixed for 1 minute. Small amounts of bentonite powders (6 g) were gradually added into the mixture, followed by 5 mixing-cooling cycles. The paste-like ink was subjected to a final defoaming cycle at 2200 rpm for 2 minutes. The other inks were formulated following the same process according to the compositions listed in Table 2.

5.3 Rheology measurements

The rheological properties of all formulations were measured using a strain-controlled rheometer (ARES G2, TA Instruments) at room temperature (25 °C). A sandblasted parallel plate geometry with a diameter of 40 mm is used and the gap between plates was set at 1.9mm or 2 mm depending on the material. An oscillatory strain amplitude sweep is carried out at a fixed oscillation frequency of 0.5 Hz with the strain amplitude changing from 0.01 % to 200 %. The data are collected at least three times in correlation mode and one time in transient mode. The correlation mode provides the first-order moduli information i.e. storage modulus (G') and loss modulus (G''). Transient mode provides the raw stress/strain waveforms, which are used to investigate the intracycle behaviour using Lissajous-Bowditch curves. The area of the elastic L-B curve represents the dissipative energy in a LAOS cycle, which can be calculated through the first-order Fourier viscous coefficient:[62]

$$E_d = \oint \sigma d\gamma = \pi G_1'' \gamma_0^2, \tag{1}$$

where G_1'' is the first-order viscous Fourier coefficient, calculated from the intensity and phase of the first-harmonic of the stress signal. γ_0 is the maximum shear strain. For a perfect plastic material under given γ_0 and σ_{max}, the energy dissipated within a cycle ($(E_d)_{pp}$) is given by:

$$(E_d)_{pp} = 4\gamma_0\sigma_{max}. \tag{2}$$

The energy dissipation ratio ϕ is defined as the actual dissipated energy divided by a perfectly plastic dissipation (square shape in L-B plot).[50,62] ϕ quantifies how closely the response of the material in a particular cycle approaches perfectly plastic flow behaviour.

$$\phi = \frac{E_d}{(E_d)_{pp}} = \frac{\pi G_1'' \gamma_0}{4\sigma_{max}}. \tag{3}$$

The value of ϕ lies between 0 and 1, representing behaviour ranging from purely elastic response ($\phi = 0$) to perfectly plastic flow response ($\phi = 1$). The trend of this metric provides useful insights linked to *printability*.[50]

5.4 Direct Ink Writing settings and drying conditions

3D models were preliminarily designed using a CAD software (Robocad 5.0), and then converted to G-code files that guide the moving path and control the extrusion rate (plunger displacement). The printer is a 3D Inks (Stillwater, OK, USA) custom-made system with an Aerotech Gantry robot. The formulations were loaded into 5 mL Luer-lock syringes. All parts were made using stainless steel nozzles with 0.51 mm inner diameter (purple, EFD Nordson). A screw bolt is used to connect the syringes plungers to the pumps. Structures were printed on a PTFE substrate layer by layer to build the complete shape. Extrusion rate was ≈ 0.2 mL s^{-1}, and the printing speed ≈ 12 mm s^{-1}. After printing, the air-dried samples were left at room temperature (25 °C) for 1 day, and transferred into a vacuum oven (80 °C) for 24 h to remove the remaining solvent and activate CC3.[9] While the freeze-dried samples were firstly frozen in liquid nitrogen and then dried at -100 °C, 0bar (Freezone 4.5, Labconco Corporation) for 48 h, followed by a second drying step in a vacuum oven (80 °C) for 24 h.

5.5 Characterization techniques

Dynamic light scattering measurements were used to determine the size distribution of the sieved CC3 and bentonite powders (dispersed in the water/ethanol (1:1) mixture) using a Malvern Mastersizer 3000 (Malvern Instruments Ltd, UK). CC3 and bentonite powders were uniaxially pressed into cylindrical pellets with an average diameter of 8±1 mm using a Specac Uniaxial press. The contact angles of the liquids (pure water, water/ethanol (1:1) mixture, and pure ethanol) were measured on the smooth surface of the pellets using the sessile drop method (KRUSS DSA100, Germany). SEM images of samples coated with a thin layer of chromium (Quorum Q-150T ES) were taken in a Hitachi S4800 SEM. PXRD patterns were collected using a Panalytical XPert PRO Alpha-1 XRD system. N_2 physisorption was measured using a Micromeritics ASAP 2020 at 55 °C, after samples were degassed under vacuum (3-5 µm Hg, 100°C) for 12 h before testing. Following the American Society for Testing and Materials (ASTM) C773-88 standard,[66] solid (bulk) cylindrical samples were prepared using the same printing settings mentioned above. The dimensions and weight of printed bulk monoliths were measured using a high-precision caliper and balance respectively, to calculate the volume and apparent density. The shrinkage in volume was calculated as $VS = 100(Vol_d - Vol_p)/Vol_d$, where Vol_d is the volume of the designed 3D models and Vol_p is the volume of the printed samples after post-processing. The mechanical compression tests were carried out using a universal testing machine (Instron 5965) with a constant loading speed of 0.8 mm min^{-1}.[66]

5.6 CFD methodology

CFD simulations were performed to investigate flow through 3D structures with varying internal features offset distance of filament and its porosity). Arranging filaments at different offsets distances in two consecutive layers creates regular grids (G=0), cubic-type arrangements (G=1), and those in between (e.g. G=0.25, 0.5 and 0.75). At the same time, the porosity ε of the filaments can be tailored through formulation design and drying conditions. The impact of filament offset spacings (G, Figure 8) and porosity (ε) on the flow patterns and pressure drop were quantified. Representative 2D unit cells (Figure 8c) were designed based on the cross-section of the printed structures (Figure 8a and b). The length l and width w of the unit cell are both 2 mm, and the diameter d of the cylinders (representing the filaments) is 0.5 mm. These dimensions are chosen based on our 3D-printed structure (Figure 8b). The offset distance g (which is normalized by the diameter of the filament d and denoted as G, $G = g/d$) between adjacent cylinders can vary from 0 mm to 0.5 mm (corresponding to G varying from 0 to 1). The porosity ε of cylinder varies from 0.22 (Da=10^{-8}) to 0.99 (Da=10^{-2}). Da is calculated by $Da = \kappa/d^2$, where κ represents the permeability given by the Kozen–Carmen equation,[70] $\kappa = \frac{1}{180}\frac{\varepsilon^3 d_p^2}{(1-\varepsilon)^2}$. Here, d_p represents the particle size in the porous cylinder ($d_p \approx 5$ μm from experimental results (Figure 5c and f)). Using periodic boundary conditions, we performed the simulations in ANSYS Fluent 20.2 for a series of geometries with different G ($0 \sim 1$) and Da ($10^{-6} \sim 10^{-2}$). An incompressible gas was used with a constant density ρ of 1.23 kg m^{-3} and viscosity μ of 1.79×10^{-5} kg (m s)$^{-1}$. The Reynolds number Re ($Re = \rho v_{av} d/\mu$, where v_{av} is

the average velocity at the inlet) is set to 0.1 as it is a representative value of common flow conditions in practical adsorption applications. For example, in 3D-printed CuO/CeO_2 monoliths at $Re \sim 0.05$-0.2 for CO conversion;[47] CO_2 adsorption capacity studies of printed zeolite structures at $Re = 0.1$;[76] and ethane/ethylene separation tests in printed ZIF-7 structures at $Re = 0.1$.[77] Re numbers for other gas adsorption experiments on reported 3D-printed structures typically range between 0.05 and 1.[34,78] Steady-state simulations are carried out for both the clear fluid domain outside the cylinders and the porous fluid domain within the cylinder. The governing equations for the clear fluid domain are given by:
continuity equation (clear fluid domain)

$$\frac{\partial v_x}{\partial x} + \frac{\partial v_y}{\partial y} = 0, \tag{4}$$

momentum equations (clear fluid domain)

$$\rho(v_x\frac{\partial v_x}{\partial x} + v_y\frac{\partial v_x}{\partial y}) = -\frac{\partial p}{\partial x} + \mu(\frac{\partial^2 v_x}{\partial x^2} + \frac{\partial^2 v_x}{\partial y^2}), \tag{5}$$

$$\rho(v_x\frac{\partial v_y}{\partial x} + v_y\frac{\partial v_y}{\partial y}) = -\frac{\partial p}{\partial y} + \mu(\frac{\partial^2 v_y}{\partial x^2} + \frac{\partial^2 v_y}{\partial y^2}), \tag{6}$$

where v_x and v_y are the velocities in the x and y directions respectively, and p is the pressure. For the porous fluid domain, the governing equations are given by the Darcy–Brinkman–Forchheimer extended model:[79–81]
continuity equation(porous fluid domain)

$$\frac{\partial v_x^s}{\partial x} + \frac{\partial v_y^s}{\partial y} = 0, \tag{7}$$

momentum equations (porous fluid domain)

$$\frac{\rho}{\varepsilon^2}(v_x^s\frac{\partial v_x^s}{\partial x} + v_y^s\frac{\partial v_x^s}{\partial y}) = -\frac{\partial p^*}{\partial x} + \frac{\mu}{\varepsilon}(\frac{\partial^2 v_x^s}{\partial x^2} + \frac{\partial^2 v_x^s}{\partial y^2}) - \frac{\mu}{\kappa}v_x^s - \frac{1.75\rho}{\sqrt{150\kappa\varepsilon^3}}\left|\overline{U}\right| v_x^s, \tag{8}$$

$$\frac{\rho}{\varepsilon^2}(v_x^s\frac{\partial v_y^s}{\partial x} + v_y^s\frac{\partial v_y^s}{\partial y}) = -\frac{\partial p^*}{\partial y} + \frac{\mu}{\varepsilon}(\frac{\partial^2 v_y^s}{\partial x^2} + \frac{\partial^2 v_y^s}{\partial y^2}) - \frac{\mu}{\kappa}v_y^s - \frac{1.75\rho}{\sqrt{150\kappa\varepsilon^3}}\left|\overline{U}\right| v_y^s. \tag{9}$$

Here, v_x^s and v_y^s are the superficial velocities (Darcy velocities) within the porous fluid domain. p^* is the intrinsic pressure and $\left|\bar{U}\right|$ is the velocity magnitude, $\left|\bar{U}\right| = \sqrt{v_x^{s2} + v_y^{s2}}$.[82,83] The geometric coordinates x and y were normalized by the length l and width w of the unit cell and denoted as x^* ($x^* = x/l$) and y^* ($y^* = y/w$) respectively. The velocity components in x- and y-directions were normalized by v_{av}, i.e., v_x/v_{av} and v_y/v_{av}, respectively. A uniform second-order quadrilateral mesh is generated using the *Mesh* module in *Workbench*. Periodic boundary conditions are applied to top-bottom and left-right edges. The cylinders are set as homogenous isotropic porous media. The mass flow rate $\dot{m}$ along the x-direction (with the value corresponding to $Re = 0.1$) is specified to drive the flow. The numerical solution is computed using the finite volume-based solver. The least squares cell based, second order and second order upwind schemes are adopted for the spatial discretization of gradient, pressure and momentum, respectively. The pressure-based solver is used with the Semi-Implicit Method for Pressure Linked Equations (SIMPLE) algorithm. The residual for the iterative convergence is set to 10^{-9} for all three variables (v_x, v_y and p). A uniform mesh with size of 4×10^{-7} m is adopted for all the simulation cases. To achieve this, a mesh independence analysis is conducted (for the solid geometry with G=0) by increasing the number of cells to assess whether the monitored variables exhibit mesh independence. The velocity component v_y in y-direction at the point P(x^* = -0.125, y^* = 0.125) and pressure drop $\triangle p$ between inlet and outlet, are selected for the mesh independence analysis. The change of v_y and $\triangle p$ and the error of each case are compared with the finest mesh respectively (Table S2 and Figure S2 in supporting information). $\triangle p$ shows

higher sensitivity relative to v_y, and convergence is achieved with a mesh size of 4×10^{-7} m and the total number of cells of 1.32×10^7, where we observed the error in the pressure drop to be as low as 0.14%.

Supporting Information

Supporting Information is available from the Wiley Online Library or from the author.

Acknowledgements

This work was supported by a UKRI Future Leaders Fellowship MR/V021117/1. Bin Ling would like to acknowledge the support from University of Liverpool and China Scholarship Council (CSC) Awards.

References

[1] Tomokazu Tozawa, James TA Jones, Shashikala I Swamy, Shan Jiang, Dave J Adams, Stephen Shakespeare, Rob Clowes, Darren Bradshaw, Tom Hasell, Samantha Y Chong, et al. Porous organic cages. *Nature materials*, 8(12):973–978, 2009.

[2] James R Holst, Abbie Trewin, and Andrew I Cooper. Porous organic molecules. *Nature chemistry*, 2(11):915–920, 2010.

[3] Dawei Zhang, Tanya K Ronson, You-Quan Zou, and Jonathan R Nitschke. Metal–organic cages for molecular separations. *Nature Reviews Chemistry*, 5(3):168–182, 2021.

[4] Ming Liu, Linda Zhang, Marc A Little, Venkat Kapil, Michele Ceriotti, Siyuan Yang, Lifeng Ding, Daniel L Holden, Rafael Balderas-Xicohténcatl, Donglin He, et al. Barely porous organic cages for hydrogen isotope separation. *Science*, 366(6465):613–620, 2019.

[5] Jolie M Lucero, Jacek B Jasinski, Miao Song, Dongsheng Li, Lili Liu, Jun Liu, James J De Yoreo, Praveen K Thallapally, and Moises A Carreon. Synthesis of porous organic cage cc3 via solvent modulated evaporation. *Inorganica Chimica Acta*, 501:119312, 2020.

[6] Tamoghna Mitra, Kim E Jelfs, Marc Schmidtmann, Adham Ahmed, Samantha Y Chong, Dave J Adams, and Andrew I Cooper. Molecular shape sorting using molecular organic cages. *Nature chemistry*, 5(4):276–281, 2013.

[7] Qilei Song, Shan Jiang, Tom Hasell, Ming Liu, Shijing Sun, Anthony K Cheetham, Easan Sivaniah, and Andrew I Cooper. Porous organic cage thin films and molecular-sieving membranes. *Advanced Materials*, 28(13):2629–2637, 2016.

[8] Tom Hasell, Samantha Y Chong, Kim E Jelfs, Dave J Adams, and Andrew I Cooper. Porous organic cage nanocrystals by solution mixing. *Journal of the American Chemical Society*, 134(1):588–598, 2012.

[9] Michael E Briggs and Andrew I Cooper. A perspective on the synthesis, purification, and characterization of porous organic cages. *Chemistry of Materials*, 29(1):149–157, 2017.

[10] Ming Liu, Marc A Little, Kim E Jelfs, James TA Jones, Marc Schmidtmann, Samantha Y Chong, Tom Hasell, and Andrew I Cooper. Acid-and base-stable porous organic cages: shape persistence and ph stability via post-synthetic "tying" of a flexible amine cage. *Journal of the American Chemical Society*, 136(21):7583–7586, 2014.

[11] Isaiah Borne, Donglin He, Stephen JA DeWitt, Ming Liu, Andrew I Cooper, Christopher W Jones, and Ryan P Lively. Polymeric fiber sorbents embedded with porous organic cages. *ACS Applied Materials & Interfaces*, 13(39):47118–47126, 2021.

[12] Wan Yun Hong, Semali P Perera, and Andrew D Burrows. Manufacturing of metal-organic framework monoliths and their application in co2 adsorption. *Microporous and Mesoporous Materials*, 214:149–155, 2015.

[13] Lalit A Darunte, Yuri Terada, Christopher R Murdock, Krista S Walton, David S Sholl, and Christopher W Jones. Monolith-supported amine-functionalized mg2 (dobpdc) adsorbents for co2 capture. *ACS applied materials & interfaces*, 9(20):17042–17050, 2017.

[14] Pia Küsgens, Alina Zgaverdea, Hans-Gerhard Fritz, Sven Siegle, and Stefan Kaskel. Metal-organic frameworks in monolithic structures. *Journal of the American Ceramic Society*, 93(9):2476–2479, 2010.

[15] Stephen JA DeWitt, Anshuman Sinha, Jayashree Kalyanaraman, Fengyi Zhang, Matthew J Realff, and Ryan P Lively. Critical comparison of structured contactors for adsorption-based gas separations. *Annual review of chemical and biomolecular engineering*, 9:129–152, 2018.

[16] Hailong Wang, Yinghua Jin, Nana Sun, Wei Zhang, and Jianzhuang Jiang. Post-synthetic modification of porous organic cages. *Chemical Society Reviews*, 50(16):8874–8886, 2021.

[17] Shane Lawson, Xin Li, Harshul Thakkar, Ali A Rownaghi, and Fateme Rezaei. Recent advances in 3d printing of structured materials for adsorption and catalysis applications. *Chemical Reviews*, 121(10):6246–6291, 2021.

[18] Vladimir Egorov, Umair Gulzar, Yan Zhang, Siobhán Breen, and Colm O'Dwyer. Evolution of 3d printing methods and materials for electrochemical energy storage. *Advanced Materials*, 32(29):2000556, 2020.

[19] Cheng Sun, Yun Wang, Michael D McMurtrey, Nathan D Jerred, Frank Liou, and Ju Li. Additive manufacturing for energy: A review. *Applied Energy*, 282:116041, 2021.

[20] Brett G Compton and Jennifer A Lewis. 3d-printing of lightweight cellular composites. *Advanced materials*, 26(34):5930–5935, 2014.

[21] Kai Huang, Hamada Elsayed, Giorgia Franchin, and Paolo Colombo. Additive manufacturing of sioc scaffolds with tunable structure-performance relationship. *Journal of the European Ceramic Society*, 41(15):7552–7559, 2021.

[22] Laura del Mazo-Barbara and Maria-Pau Ginebra. Rheological characterisation of ceramic inks for 3d direct ink writing: A review. *Journal of the European Ceramic Society*, 41(16):18–33, 2021.

[23] Esther García-Tuñon, Suelen Barg, Jaime Franco, Robert Bell, Salvador Eslava, Eleonora D'Elia, Robert Christopher Maher, Francisco Guitian, and Eduardo Saiz. Printing in three dimensions with graphene. *Advanced materials*, 27(10):1688–1693, 2015.

[24] Yanqiu Jiang, Zhen Xu, Tieqi Huang, Yingjun Liu, Fan Guo, Jiabin Xi, Weiwei Gao, and Chao Gao. Direct 3d printing of ultralight graphene oxide aerogel microlattices. *Advanced Functional Materials*, 28(16):1707024, 2018.

[25] Xiaocong Tian. Direct ink writing of 2d material-based supercapacitors. *2D Materials*, 9(1):012001, 2021.

[26] Ezra Feilden, Claudio Ferraro, Qinghua Zhang, Esther García-Tuñón, Eleonora D'Elia, Finn Giuliani, Luc Vandeperre, and Eduardo Saiz. 3d printing bioinspired ceramic composites. *Scientific reports*, 7(1):13759, 2017.

[27] Kunpeng Cai, Jingbo Sun, Qi Li, Rui Wang, Bo Li, and Ji Zhou. Direct-writing construction of layered meshes frománanoparticles-vaseline composite inks: rheological properties andástructures. *Applied Physics A*, 102:501–507, 2011.

[28] Victoria G Rocha, Eduardo Saiz, Iuliia S Tirichenko, and Esther García-Tuñón. Direct ink writing advances in multi-material structures for a sustainable future. *Journal of Materials Chemistry A*, 8(31):15646–15657, 2020.

[29] Harshul Thakkar, Stephen Eastman, Amit Hajari, Ali A Rownaghi, James C Knox, and Fateme Rezaei. 3d-printed zeolite monoliths for co2 removal from enclosed environments. *ACS applied materials & interfaces*, 8(41):27753–27761, 2016.

[30] Jasper Lefevere, Benjamin Claessens, Steven Mullens, Gino Baron, Julien Cousin-Saint-Remi, and Joeri FM Denayer. 3d-printed zeolitic imidazolate framework structures for adsorptive separations. *ACS Applied Nano Materials*, 2(8):4991–4999, 2019.

[31] Harshul Thakkar, Stephen Eastman, Qasim Al-Naddaf, Ali A Rownaghi, and Fateme Rezaei. 3d-printed metal–organic framework monoliths for gas adsorption processes. *ACS applied materials & interfaces*, 9(41):35908–35916, 2017.

[32] Esther García-Tuñón, Ezra Feilden, Han Zheng, Eleonora D'Elia, Alan Leong, and Eduardo Saiz. Graphene oxide: an all-in-one processing additive for 3d printing. *ACS applied materials & interfaces*, 9(38):32977–32989, 2017.

[33] Andrew Corker, Henry C-H Ng, Robert J Poole, and Esther García-Tuñón. 3d printing with 2d colloids: Designing rheology protocols to predict 'printability'of soft-materials. *Soft Matter*, 15(6):1444–1456, 2019.

[34] Sarah Couck, Julien Cousin-Saint-Remi, Stijn Van der Perre, Gino V Baron, Clara Minas, Patrick Ruch, and Joeri FM Denayer. 3d-printed sapo-34 monoliths for gas separation. *Microporous and Mesoporous Materials*, 255:185–191, 2018.

[35] Jérémy Dhainaut, Mickaele Bonneau, Ryota Ueoka, Kazuyoshi Kanamori, and Shuhei Furukawa. Formulation of metal–organic framework inks for the 3d printing of robust microporous solids toward high-pressure gas storage and separation. *ACS applied materials & interfaces*, 12(9):10983–10992, 2020.

[36] Weiwei Kang, Yan Cui, Lei Qin, Yongzhen Yang, Zongbin Zhao, Xuzhen Wang, and Xuguang Liu. A novel robust adsorbent for efficient oil/water separation: Magnetic carbon nanospheres/graphene composite aerogel. *Journal of hazardous materials*, 392:122499, 2020.

[37] Shane Lawson, Qasim Al-Naddaf, Anirduh Krishnamurthy, Marc St Amour, Connor Griffin, Ali A Rownaghi, James C Knox, and Fateme Rezaei. Utsa-16 growth within 3d-printed co-kaolin monoliths with high selectivity for co2/ch4, co2/n2, and co2/h2 separation. *ACS applied materials & interfaces*, 10(22):19076–19086, 2018.

[38] Carlos A Grande, Richard Blom, Vesna Middelkoop, Dorota Matras, Antonis Vamvakeros, Simon DM Jacques, Andrew M Beale, Marco Di Michiel, Kari Anne Andreassen, and Aud M Bouzga. Multiscale investigation of adsorption properties of novel 3d printed utsa-16 structures. *Chemical Engineering Journal*, 402:126166, 2020.

[39] Jennifer A Lewis. Colloidal processing of ceramics. *Journal of the American Ceramic Society*, 83(10):2341–2359, 2000.

[40] Sarah Couck, Jasper Lefevere, Steven Mullens, Lidia Protasova, Vera Meynen, Gert Desmet, Gino V Baron, and Joeri FM Denayer. Co2, ch4 and n2 separation with a 3dfd-printed zsm-5 monolith. *Chemical Engineering Journal*, 308:719–726, 2017.

[41] Shane Lawson and Fateme Rezaei. Effects of process parameters on co2/h2 separation performance of 3d-printed mof-74 monoliths. *ACS Sustainable Chemistry & Engineering*, 9(32):10902–10912, 2021.

[42] Shuang Wang, Pu Bai, Mingzhe Sun, Wei Liu, Dongdong Li, Wenzheng Wu, Wenfu Yan, Jin Shang, and Jihong Yu. Fabricating mechanically robust binder-free structured zeolites by 3d printing coupled with zeolite soldering: a superior configuration for co2 capture. *Advanced Science*, 6(17):1901317, 2019.

[43] Ximeng Liu, Gwendolyn JH Lim, Yuxiang Wang, Lei Zhang, Dinesh Mullangi, Yue Wu, Dan Zhao, Jun Ding, Anthony K Cheetham, and John Wang. Binder-free 3d printing of covalent organic framework (cof) monoliths for co2 adsorption. *Chemical Engineering Journal*, 403:126333, 2021.

[44] John N Stuecker, James E Miller, Robert E Ferrizz, Jason E Mudd, and Joseph Cesarano. Advanced support structures for enhanced catalytic activity. *Industrial & engineering chemistry research*, 43(1):51–55, 2004.

[45] Saeed Hajimirzaee, David Shaw, Paul Howard, and Aidan M Doyle. Industrial scale 3d printed catalytic converter for emissions control in a dual-fuel heavy-duty engine. *Chemical Engineering Science*, 231:116287, 2021.

[46] Saeed Hajimirzaee and Aidan M Doyle. 3d printed catalytic converters with enhanced activity for low-temperature methane oxidation in dual-fuel engines. *Fuel*, 274:117848, 2020.

[47] Cristian Y Chaparro-Garnica, Pepe Jorda-Faus, Esther Bailon-Garcia, Raul Ocampo-Perez, Carlos G Aguilar-Madera, Arantxa Davo-Quinonero, Dolores Lozano-Castello, and Agustin Bueno-Lopez. Customizable heterogeneous catalysts: nonchanneled advanced monolithic supports manufactured by 3d-printing for improved active phase coating performance. *ACS Applied Materials & Interfaces*, 12(49):54573–54584, 2020.

[48] Benjamin Claessens, Nicolas Dubois, Jasper Lefevere, Steven Mullens, Julien Cousin-Saint-Remi, and Joeri FM Denayer. 3d-printed zif-8 monoliths for biobutanol recovery. *Industrial & Engineering Chemistry Research*, 59(18):8813–8824, 2020.

[49] Jiangtao Yu, Jie Zhu, Linlin Chen, Yanhong Chao, Wenshuai Zhu, and Zhichang Liu. A review of adsorption materials and their application of 3d printing technology in the separation process. *Chemical Engineering Journal*, page 146247, 2023.

[50] Esther Garcia-Tunon, Rishav Agrawal, Bin Ling, and David J. C. Dennis. Fourier-transform rheology and printability maps of complex fluids for three-dimensional printing. *Physics of Fluids*, 35(1):017113, 01 2023.

[51] Ying Liu, Matthew Hildner, Omkar Roy, William A Van den Bogert, James Lorenz, Maude Desroches, Kurt Koppi, Albert Shih, and Ronald G Larson. On the selection of rheological tests for the prediction of 3d printability. *Journal of Rheology*, 67(4):791–791, 2023.

[52] Tom Hasell, Marcin Miklitz, Andrew Stephenson, Marc A Little, Samantha Y Chong, Rob Clowes, Linjiang Chen, Daniel Holden, Gareth A Tribello, Kim E Jelfs, et al. Porous organic cages for sulfur hexafluoride separation. *Journal of the American Chemical Society*, 138(5):1653–1659, 2016.

[53] Angelika Basch and Simona Strnad. Substrate-induced coagulation (sic) of nano-disperse alumina in non-aqueous media: The dispersibility and stability of alumina in n-methyl-2-pyrrolidinone. *Colloids and Surfaces A: Physicochemical and Engineering Aspects*, 374(1-3):9–12, 2011.

[54] Shane Lawson, Connor Griffin, Kambria Rapp, Ali A Rownaghi, and Fateme Rezaei. Amine-functionalized mil-101 monoliths for co2 removal from enclosed environments. *Energy & Fuels*, 33(3):2399–2407, 2019.

[55] Rouja Ivanova, Björn Lindman, and Paschalis Alexandridis. Evolution in structural polymorphism of pluronic f127 poly (ethylene oxide)- poly (propylene oxide) block copolymer in ternary systems with water and pharmaceutically acceptable organic solvents: From "glycols" to "oils". *Langmuir*, 16(23):9058–9069, 2000.

[56] Bana Shriky, Adrian Kelly, Mohammad Isreb, Maksims Babenko, Najet Mahmoudi, Sarah Rogers, Olga Shebanova, Tim Snow, and Tim Gough. Pluronic f127 thermosensitive injectable smart hydrogels for controlled drug delivery system development. *Journal of colloid and interface science*, 565:119–130, 2020.

[57] Jianhua Ma, Peng Wang, Lei Dong, Ruan Yingbo, and Lu Hongbin. Highly conductive, mechanically strong graphene monolith assembled by three-dimensional printing of large graphene oxide. *Journal of Colloid and Interface Science*, 534:12–19, 2019.

[58] Daniel A Rau, Christopher B Williams, and Michael J Bortner. Rheology and printability: A survey of critical relationships for direct ink write materials design. *Progress in Materials Science*, page 101188, 2023.

[59] Shelbie A Legett, Xavier Torres, Andrew M Schmalzer, Adam Pacheco, John R Stockdale, Samantha Talley, Tom Robison, and Andrea Labouriau. Balancing functionality and printability: High-loading polymer resins for direct ink writing. *Polymers*, 14(21):4661, 2022.

[60] Kyu Hyun, Sook Heun Kim, Kyung Hyun Ahn, and Seung Jong Lee. Large amplitude oscillatory shear as a way to classify the complex fluids. *Journal of Non-Newtonian Fluid Mechanics*, 107(1-3):51–65, 2002.

[61] Daniela Coblas, Diana Broboana, and Corneliu Balan. Correlation between large amplitude oscillatory shear (laos) and steady shear of soft solids at the onset of the fluid rheological behavior. *Polymer*, 104:215–226, 2016.

[62] Randy H Ewoldt, Peter Winter, Jason Maxey, and Gareth H McKinley. Large amplitude oscillatory shear of pseudoplastic and elastoviscoplastic materials. *Rheologica acta*, 49:191–212, 2010.

[63] Dong-Wei Wang, Cheng Zhu, Chao-Sheng Tang, Qing Cheng, Sheng-Jie Li, and Bin Shi. Experimental study on shrinkage characteristics of compacted bentonite–sand mixtures. *Bulletin of Engineering Geology and the Environment*, 83(1):43, 2024.

[64] Xian Zhang, Hao Yi, Haoyu Bai, Yunliang Zhao, Fanfei Min, and Shaoxian Song. Correlation of montmorillonite exfoliation with interlayer cations in the preparation of two-dimensional nanosheets. *Rsc Advances*, 7(66):41471–41478, 2017.

[65] N Othman, H Ismail, and M Mariatti. Effect of compatibilisers on mechanical and thermal properties of bentonite filled polypropylene composites. *Polymer Degradation and Stability*, 91(8):1761–1774, 2006.

[66] ASTM C773-88. Standard test method for compressive (crushing) strength of fired whiteware materials, 2020.

[67] Mike Ashby. Hybrid materials to expand the boundaries of material-property space. *Journal of the American Ceramic Society*, 94:s3–s14, 2011.

[68] Chih-Hsiung Gary Cheng. *The effects of streamline curvature and swirl on turbulent flows in curved ducts*. University of Kansas, 1991.

[69] Henry Darcy. *Les fontaines publiques de la ville de Dijon: exposition et application des principes à suivre et des formules à employer dans les questions de distribution d'eau*, volume 1. Victor dalmont, 1856.

[70] Donald A Nield, Adrian Bejan, et al. *Convection in porous media*, volume 3. Springer, 2006.

[71] Dingyue Hu, Jinjin Zhang, and Ming Liu. Recent advances in the applications of porous organic cages. *Chemical Communications*, 58(81):11333–11346, 2022.

[72] Karim Adil, Youssef Belmabkhout, Renjith S Pillai, Amandine Cadiau, Prashant M Bhatt, Ayalew H Assen, Guillaume Maurin, and Mohamed Eddaoudi. Gas/vapour separation using ultra-microporous metal–organic frameworks: insights into the structure/separation relationship. *Chemical Society Reviews*, 46(11):3402–3430, 2017.

[73] Wenjing Wang, Kongzhao Su, and Daqiang Yuan. Porous organic cages for gas separations. *Materials Chemistry Frontiers*, 2023.

[74] Ming Liu, Linjiang Chen, Scott Lewis, Samantha Y Chong, Marc A Little, Tom Hasell, Iain M Aldous, Craig M Brown, Martin W Smith, Carole A Morrison, et al. Three-dimensional protonic conductivity in porous organic cage solids. *Nature Communications*, 7(1):12750, 2016.

[75] Miao Xu and Fanzhi Yang. Transition metal nanoparticles-catalyzed organic reactions within porous organic cages. *ChemCatChem*, 14(12):e202200183, 2022.

[76] Shane Lawson, Busuyi Adebayo, Chad Robinson, Qasim Al-Naddaf, Ali A Rownaghi, and Fateme Rezaei. The effects of cell density and intrinsic porosity on structural properties and adsorption kinetics in 3d-printed zeolite monoliths. *Chemical Engineering Science*, 218:115564, 2020.

[77] Harshul Thakkar, Qasim Al-Naddaf, Natalia Legion, Morgan Hovis, Anirudh Krishnamurthy, Ali A Rownaghi, and Fateme Rezaei. Adsorption of ethane and ethylene over 3d-printed ethane-selective monoliths. *ACS Sustainable Chemistry & Engineering*, 6(11):15228–15237, 2018.

[78] Vesna Middelkoop, Kai Coenen, Jonathan Schalck, Martin Van Sint Annaland, and Fausto Gallucci. 3d printed versus spherical adsorbents for gas sweetening. *Chemical Engineering Journal*, 357:309–319, 2019.

[79] S Bhattacharyya, S Dhinakaran, and Arzhang Khalili. Fluid motion around and through a porous cylinder. *Chemical Engineering Science*, 61(13):4451–4461, 2006.

[80] P Yu, Y Zeng, TS Lee, HX Bai, and HT Low. Wake structure for flow past and through a porous square cylinder. *International Journal of Heat and Fluid Flow*, 31(2):141–153, 2010.

[81] Saqib Jamshed, Rohit Kharbanda, and Amit Kumar Dhiman. Study of flow through and around a pair of porous cylinders covering steady and unsteady regimes. *Physics of Fluids*, 34(10), 2022.

[82] DA Nield. The limitations of the brinkman-forchheimer equation in modeling flow in a saturated porous medium and at an interface. *International Journal of Heat and Fluid Flow*, 12(3):269–272, 1991.

[83] Chin-Tsau Hsu and Ping Cheng. Thermal dispersion in a porous medium. *International Journal of Heat and Mass Transfer*, 33(8):1587–1597, 1990.